OPTOSKY
Spectroscopy Solutions

Datasheet

ATHF8100

UV Fluorescence Hyperspectral Imager

1503 Bld. A04, 3rd Software Park, Jimei, Xiamen, 361005, China
Tel: +86-592-6102588

OPTOSKY Spectroscopy Solutions

Datasheet

UV Fluorescence Hyperspectral Imager ATHF8100

Features

- Excitation wavelength: 275, 310, 365 or 405nm, others can be customized.
- Real-time autofocus, auto scanning, auto stitching.
- Optimum number of spatial channels: 3000.
- Maximum number of spectral channels: 4096.
- Push-broom scanning imaging method. No limit to scan length.
- Full-band fluorescence and spatial simultaneous imaging.
- Best fluorescence spectral resolution: better than 1.5nm.
- Large area motorized scanning platform.
- Transmission grating spectrum, higher sensitivity.
- Ultra-high performance fluorescence detector, higher SNR.
- Powerful image acquisition and analysis software.
- Integrated frame, excellent stability.
- Modular structure, multi-function combination.

Application

- Biomedicine, Early Tumor Judgment
- Plant health, seed health
- Algae classification
- Medicine and other fields
- Material science

Description

ATHF8100 is an auto-focusing, auto-scanning large-area fluorescence hyperspectral spectrometer developed by OPTOSKY. Excitation light is ultraviolet light or blue light. It analyzes the spectrum of the emitted light and performs imaging at the same time, so as to realize the fluorescence spectrum at different positions test. It can both perform spatial imaging and scan out the fluorescence spectrum at each location.

Covering the UV-Vis band, high spectral resolution, suitable for mission-critical applications ranging from biomedicine to forensic science to UV measurement.

ATHF8100 is equipped with a highly stable autofocus system that can dynamically adjust the focus of the target in real time to achieve the best imaging effect.

ATHF8100 is connected to the computer through the USB 3.0 interface, and there is also advanced and easy-to-use PC-side control software, which can achieve perfect experimental operation.

Model	Illustrate
ATHF8100	4096×3000, cooled detector
ATHF8100SCM	2048×2048, cooled sCMOS detector

1503 Bld. A04, 3rd Software Park, Jimei, Xiamen, 361005, China
Tel: +86-592-6102588

1. Selection guide

Model	Feature
ATHF8100	Auto focus, auto scanning, auto fluorescence scanning imaging
ATHF8100SCM	2048×2048, cooled sCMOS detector, with auto focusing by default focus, auto scanning, auto fluorescence scanning imaging

2. Performance parameters

Parameters	ATHF8100	ATHF8100SCM
Excitation parameters		
Excitation wavelength	Two of 275, 310, 365, 405nm, other excitation wavelengths can be customized	
Excitation light source	Long-life UV LED light source, UV laser light source optional	
Maximum excitation power	25W, optional 500W	
Fluorescence receiving part parameters		
Spectral detection range	400-1000nm range full spectrum	400-1000nm range full spectrum
Maximum number of fluorescence channels	3000	2048
Fluorescence spectral resolution (FWHM)	1.5nm	1.5nm
Number of imaging space channels	4096	2048
Spatial resolution	110μm	110μm
Detector	CCD detector	Cooled sCMOS detector
Detector resolution	4096×3000	2048×2048
Refrigeration temperature	Uncooled	5℃
Integration time	1ms-30min	
Detector interface	USB3.0	
Dynamic range	≥60dB	
Maximum frame rate	30Hz	80Hz
Visible light imaging system		
Light source	LED white light source	
Imaging camera	5 million pixel digital camera	
Camera interface	USB2.0	
Stage		
Focusing device	Manual focus or automatic focus, and a focus upper limit device	
Stage	Steel wire transmission stage (X axis does not protrude), double clip structure	
Stage area	500×300mm	
Z axis (electric control, auto focus)		

1503 Bld. A04, 3rd Software Park, Jimei, Xiamen, 361005, China
Tel: +86-592-6102588

Focus accuracy	≤±0.2μm
Focus speed	No more than 10s
Dimensions	2000×810×8200mm
Weight	49.3Kg
Software part	
Function	Visual imaging and real-time fluorescence spectral detection

3. Principle diagram of near-infrared second-region fluorescence imaging

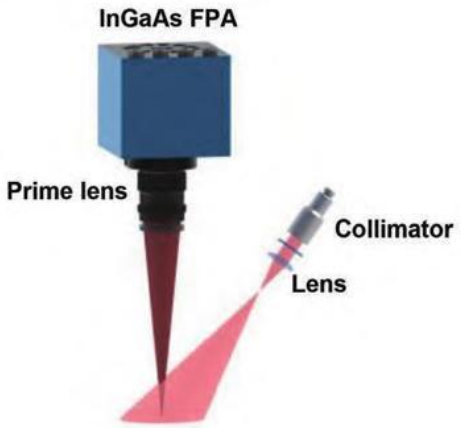

4. Application case

4.1. Early detection of grape downy mildew

Grape downy mildew is a fungal disease caused by grape downy mildew (plasmopara viticola, PV). The disease has a strong ability to infect and spread quickly, so early control is the key. If the early detection of downy mildew infection can be realized during the incubation period, a control plan can be formulated early, the spread and prevalence of downy mildew can be blocked, and the quality and yield of grapes can be guaranteed. However, during the incubation period of downy mildew without symptoms, field observation cannot judge the infection of downy mildew. The polymerase chain reaction (PCR) technology that has emerged in recent years can accurately determine the pathogenic bacteria through DNA quantitative amplification technology, and through the detection of pathogenic bacteria relative biomass can be used to determine the degree of infection, but the preparation of samples by PCR technology is time-consuming and laborious, and must be completed in the laboratory, which cannot be quickly and non-destructively detected in the field before downy mildew disease. As a new technology for non-destructive detection, pulse amplitude-modulated chloro-phyll fluorescence (PAM-ChlF) imaging technology is widely used in the early detection of plant diseases. PAM-ChlF imaging technology can effectively detect a variety of plant diseases. However, existing studies mostly use a single parameter and image for analysis, lack of chlorophyll fluorescence data for multiple days from the invasion of downy mildew to the manifestation of symptoms, and have not yet established a comprehensive method for the early detection of downy mildew that can accurately detect downy mildew.

1503 Bld. A04, 3rd Software Park, Jimei, Xiamen, 361005, China
Tel: +86-592-6102588

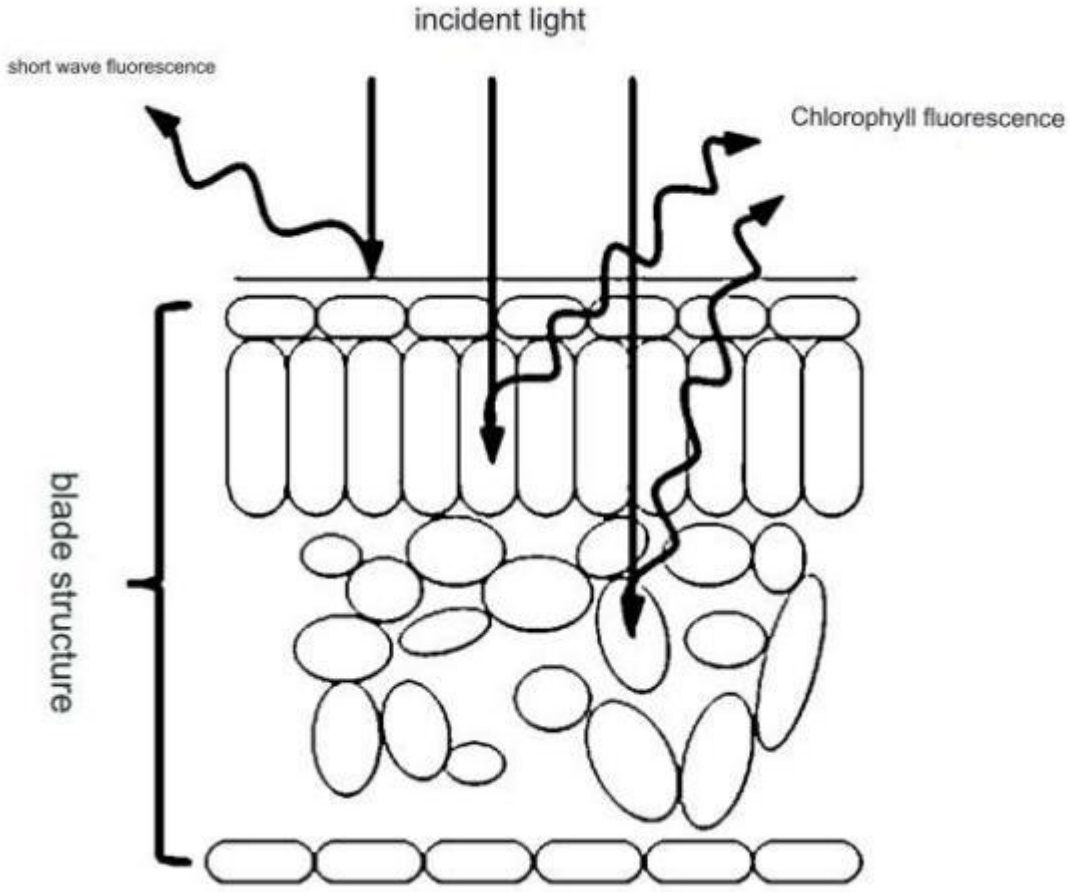

Figure 1 Schematic diagram of chlorophyll fluorescence imaging.

Grape downy mildew poses a serious threat to grape production, and early prevention and control is the key to controlling downy mildew. In order to conduct early detection of the disease, the relative biomass of downy mildew obtained by PCR detection was used as the basis for downy mildew infection. During the continuous changes in the three photosynthetic physiological states from dark adaptation to light adaptation to dark relaxation, chlorophyll fluorescence images of 80 artificially inoculated downy mildew leaves and 80 healthy control leaves were collected for 6 consecutive days. The differences in chlorophyll fluorescence kinetic curves, parameter images and parameter values of healthy and inoculated leaves were compared, and one-way analysis of variance was used to evaluate the sensitivity of chlorophyll fluorescence parameters to downy mildew infection, the optimal feature subset of chlorophyll fluorescence parameters was screened, and a machine learning classifier was used to build a downy mildew early detection model. The results showed that with the number of days after inoculation (DPI), the degree of downy mildew infection continues to deepen. The chlorophyll fluorescence kinetic curves, parameter images and parameter values of healthy and inoculated leaves are significantly different from 2DPI ($p < 0.05$). Downy mildew infection reduces leaf photochemical quenching rate (Rfd becomes smaller),

1503 Bld. A04, 3rd Software Park, Jimei, Xiamen, 361005, China
Tel: +86-592-6102588

photosynthetic efficiency decreases (Fv/Fm becomes smaller), leaf vitality and photoprotection capabilities decline (NPQ and qN become smaller), and more light energy absorbed by the leaves is released in the form of fluorescence (Ft and Fm become larger). Zhao Zhang et al. published "Early Detection of Grape Downy Mildew with Chlorophyll Fluorescence Imaging Technology" in "Spectroscopy and Spectral Analysis". The experiment was carried out successfully.

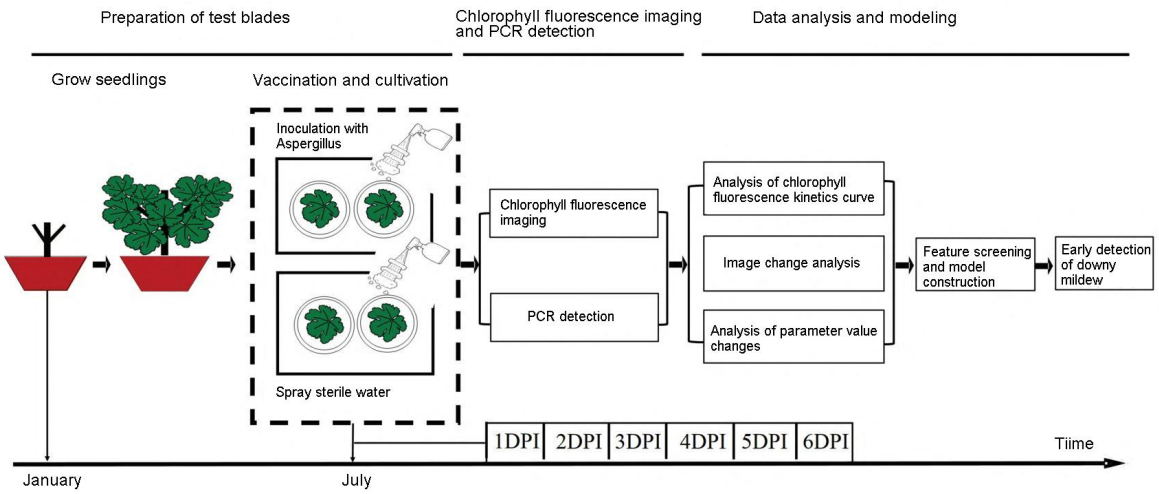

Figure 2 Experiment flow chart.

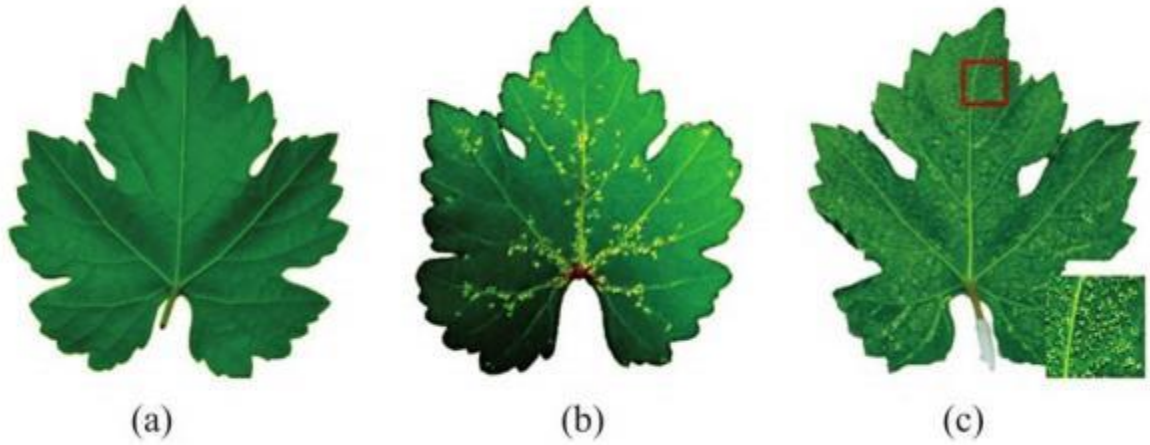

Figure 3 Healthy leaves and inoculated leaves on the 6th day after inoculation (a) healthy leaves; (b) regional disease; (c) whole leaf disease.

1503 Bld. A04, 3rd Software Park, Jimei, Xiamen, 361005, China
Tel: +86-592-6102588

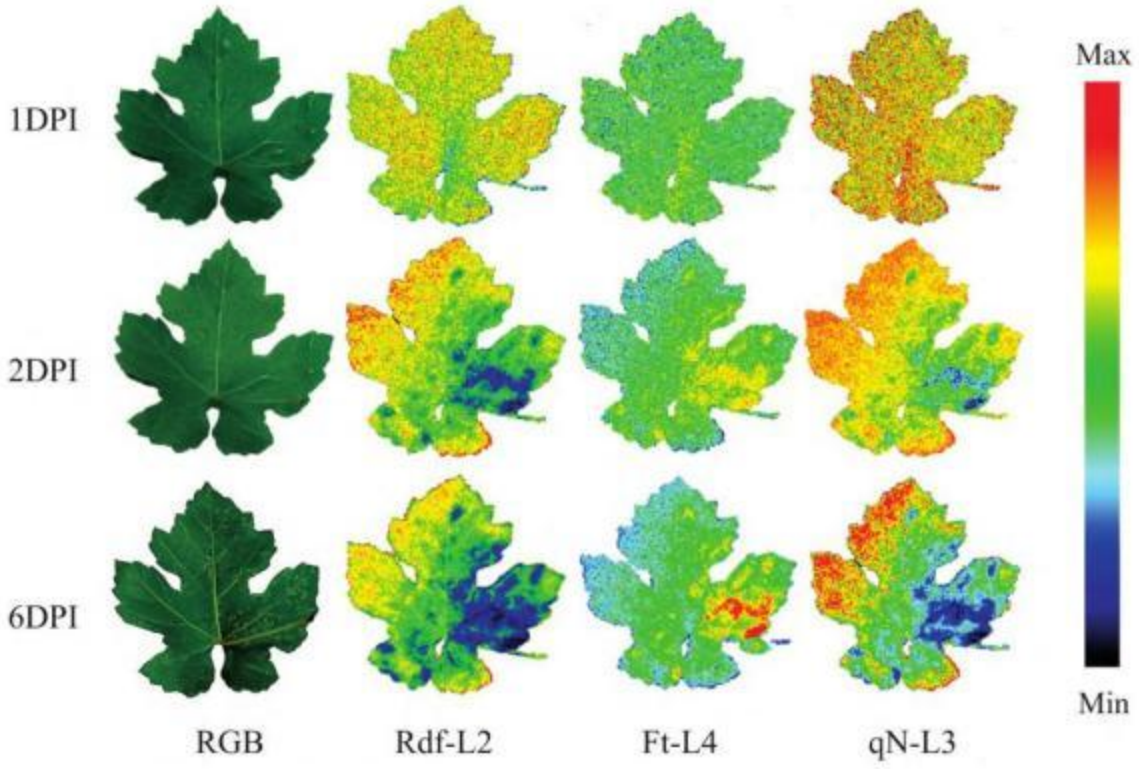

Figure 4 RGB image and chlorophyll fluorescence parameter image of leaves inoculated with downy mildew.

Taking inoculated and healthy control grape leaves as the research object, with the goal of early detection of downy mildew on grapes, the PCR detection data were used as the basis for downy mildew infection, which verified the feasibility of PAM-ChlF imaging technology for early detection of downy mildew. During the continuous changes in the three photosynthetic physiological states from dark adaptation to light adaptation to dark relaxation, 98 fluorescence parameter images of healthy and inoculated grape leaves were obtained for 6 consecutive days. Through data analysis and research, it was found that:

(1) The PCR detection results show that the infection degree of the grafted leaves is deepening. At 2DPI, the chlorophyll fluorescence image can detect the infection from the front of the leaves. The lesion area appears spatiotemporally heterogeneous, and the average parameter values of healthy and inoculated leaves are significantly different ($p < 0.05$).

(2) As the days of inoculation increase, downy mildew infection causes the photochemical quenching rate of inoculated leaves to decrease (Rfd becomes smaller), photosynthetic efficiency decreases (Fv/Fm becomes smaller), and leaf vitality and photoprotection ability decline (NPQ and qN become smaller), more light energy absorbed by the leaves is released in the form of fluorescence (Ft and Fm become larger).

(3) The early detection model of chlorophyll fluorescence parameters based on feature algorithms (SFFS and Relief) and machine learning classifiers (LR, LDA and BP) successfully achieved early detection of downy mildew, among which the feature subset optimized based on the SFFS algorithm (qN- L 3 , Rfd - L 2 , NPQ - L 1 and Fv/Fm- D 1) and the SFFS-BP model of the BP neural network classifier have an accuracy of 83.75% for the identification of healthy and inoculated leaves on 3DPI. The experimental period lasted

1503 Bld. A04, 3rd Software Park, Jimei, Xiamen, 361005, China
Tel: +86-592-6102588

for 6 consecutive days, and the average accuracy reached 85.94%.

4.2. Detection of stimulus cryptocystosis

Cryptocaryoniasis is a common and important parasitic disease in marine fish. Larvae are a key stage in the development of cryptocaryonis. They directly infect the skin and gills of bony fishes. Generally, the stages that do not develop into larvae are called cysts. which develop into swimming larvae called spores. At present, the author has realized the microscopic hyperspectral imaging of cysts (stimulating Cryptocaryonia), which can be used to analyze the material composition in the body.

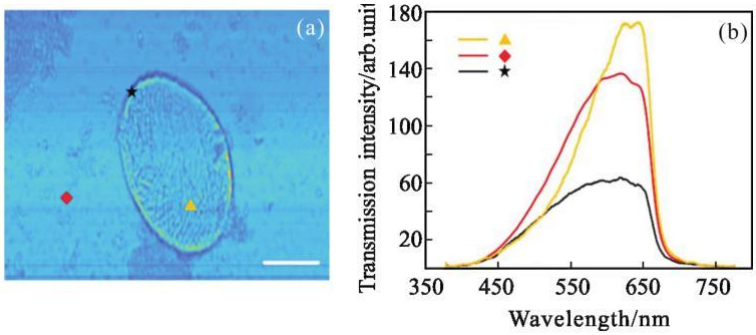

Figure 5 Hyperspectral image of a cyst (a marine fish infectious disease vector stimulating Cryptosporidium) under a 40x microscope objective (Scale bar: 30μm); (b) Spectrum of two locations within the cyst and the surrounding environment.

4.3. Research on the application of hyperspectral fluorescence imaging technology in identifying early rotten navel oranges (Li Jiangbo of Zhejiang University, etc.)

Rot is the most common and serious disease that occurs in citrus fruits. Automated detection of early rotten fruits can help improve the market competitiveness of the fruit processing industry. However, there is currently no effective automated detection technology. Taking navel orange as the research object, fluorescence hyperspectral imaging was used to detect early fruit rot. The optimal index OIF theory is used to identify the optimal band combination (498.6nm and 591.4nm) for rotten fruit. Based on the optimal wavelength ratio image and double threshold segmentation algorithm, the recognition rate reaches 100%. Research shows that this method can effectively overcome the impact of the fluorescence effect of stem-damaged fruits and fruit stems induced by ultraviolet rays on the identification of rotten fruits. This research lays the foundation for the development of an online detection system for early rotten fruits based on multispectral imaging technology.

Hyperspectral imaging technology, especially fluorescence imaging technology, has been gradually introduced into the field of non-destructive testing of agricultural product quality and safety due to its full-band continuous spectral information and the ability to identify different chemical components of target objects. Relevant studies have shown that the band ratio algorithm not only has the advantage of reducing uneven illumination caused by the curved surface of spherical fruits, but also can effectively enhance the differences between different components and provide some unique information that cannot be obtained from single-band or color images. The main purpose of this study is to develop an effective early rotten fruit detection algorithm using hyperspectral fluorescence imaging technology

1503 Bld. A04, 3rd Software Park, Jimei, Xiamen, 361005, China
Tel: +86-592-6102588

combined with band ratio detection theory to lay the foundation for rapid detection of rotten fruit on citrus fruit grading and packaging lines.

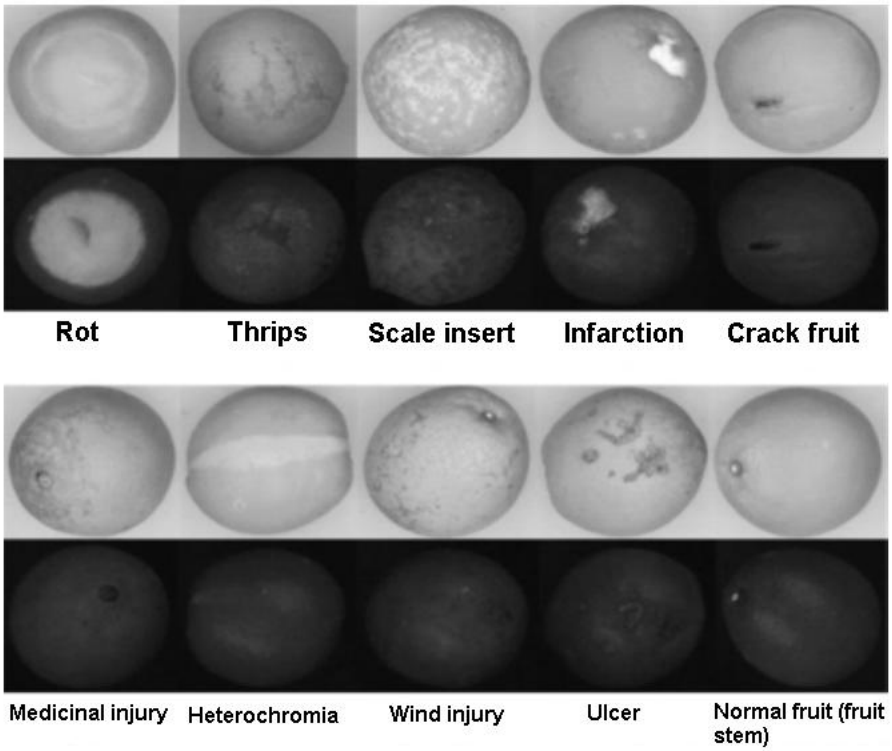

Figure 6 Comparison of visible light and fluorescence images of navel oranges in different states.

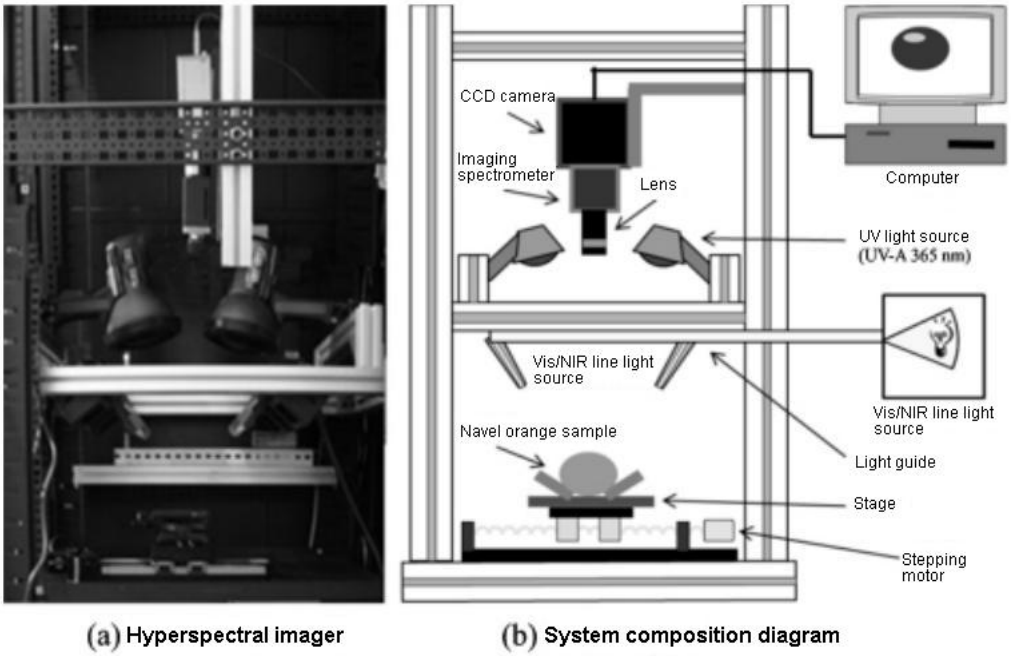

Figure 7 The fluorescence hyperspectral imaging system used in the experiment, the excitation light is 365nm.

1503 Bld. A04, 3rd Software Park, Jimei, Xiamen, 361005, China
Tel: +86-592-6102588

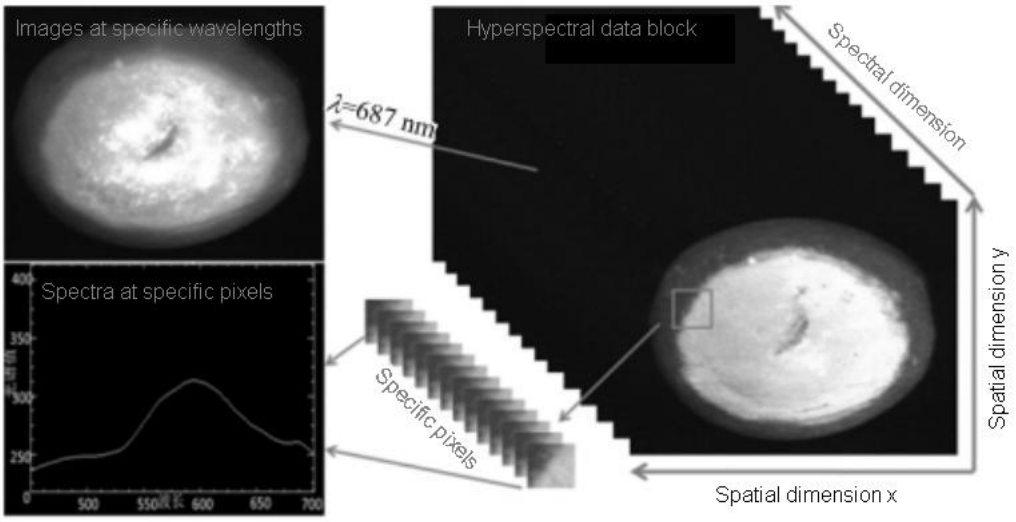

Figure 8 Hyperspectral image data.

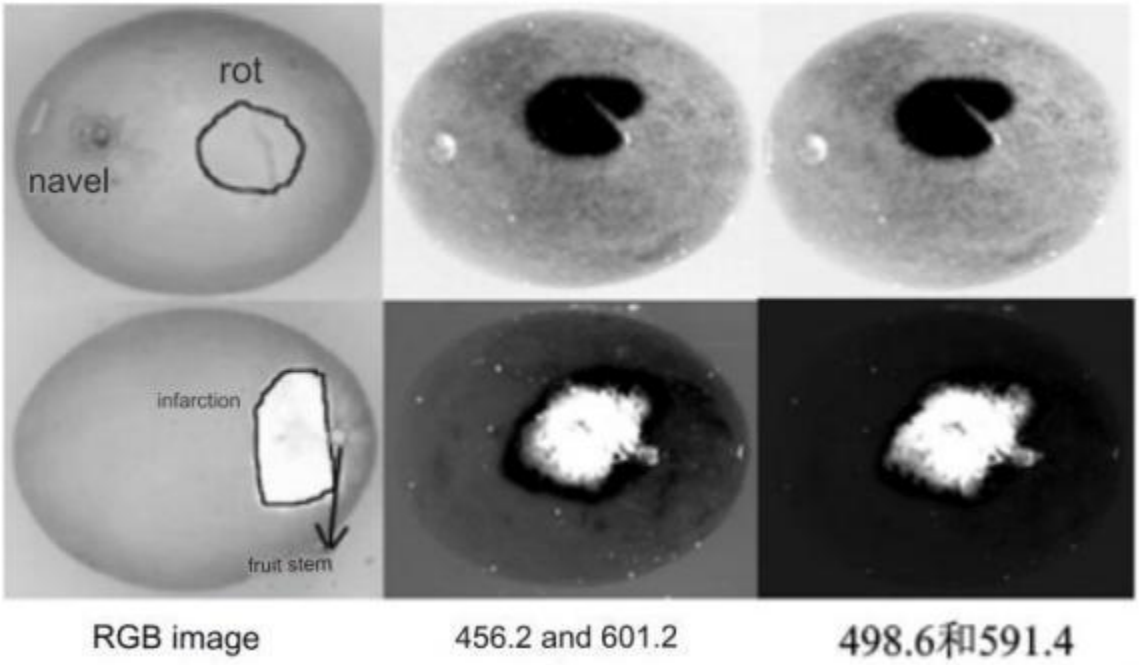

Figure 9 Hyperspectral image inversion results.

The potential of using fluorescence hyperspectral imaging technology to detect early rotten fruits was explored using navel oranges as the research object. The optimal index OIF theory was used to obtain the optimal band combination for identifying rotten fruit, achieve dimensionality reduction of high-dimensional data, and quickly determine the characteristic wavelength. Based on the characteristic wavelength ratio image and double threshold segmentation algorithm, an overall 100% rotten fruit recognition rate was achieved. The use of dual thresholds better avoids the impact of the fluorescence effect of stem defects on the detection of rotten fruits, thereby reducing system and algorithm costs.

1503 Bld. A04, 3rd Software Park, Jimei, Xiamen, 361005, China
Tel: +86-592-6102588

Although this test was developed for navel oranges, this theory can also be extended to the detection of other citrus and rotten fruits.

4.4. Research on prediction of storage time of packaged fresh pork based on UV fluorescence imaging

The food industry's demand for detection methods is increasing day by day. Not only the detection of surface defects in food and the detection of foreign matter in packaging require rapid and non-destructive testing, but even the internal quality testing of food also strives to be non-contact, rapid and objective. Products with fluorescent properties produced during lipid oxidation reactions can be used as indirect indicators of the freshness of foods containing oils. Studies have examined the ultraviolet fluorescence wavelength distribution and fluorescence intensity of minced pork and ground turkey as a measure of the freshness of minced meat products, and pointed out that protoporphyrin and zinc protoporphyrin are the main luminescent components of the fluorescent product in the lipid oxygenation process. Studies have shown that the production of zinc protoporphyrin in minced pork is inhibited in a high-oxygen environment and accumulates as the storage time increases under vacuum conditions.

In the "Research on Prediction of Storage Time of Packaged Fresh Pork Based on Ultraviolet Fluorescence Imaging" published by Xiwei Wang and others from the School of Mechanical and Electrical Engineering of Nanjing Forestry University, according to the characteristics of lipid oxidation fluorescence metabolites increasing with storage time during pork storage, a set of storage time analysis methods for packaged fresh pork based on the principle of ultraviolet fluorescence imaging were developed. Select fat and lean pork belly with skin to collect visible light color images and ultraviolet fluorescence images. The image is segmented into the muscle area, backfat, fleshy skin, and fluorescent areas, and then the area percentage of the image occupied by the fluorescent areas in the backfat and fleshy skin parts is proposed as a freshness prediction index. The research results show that the relationship between the detection index and the storage time is consistent with the exponential function growth law, the coefficient of determination R^2 =0.9336, and the root mean square error RMSE =5.186, indicating that this method can be used to determine the storage time of packaged fresh pork in specific parts and under certain conditions. Non-contact rapid non-destructive testing.

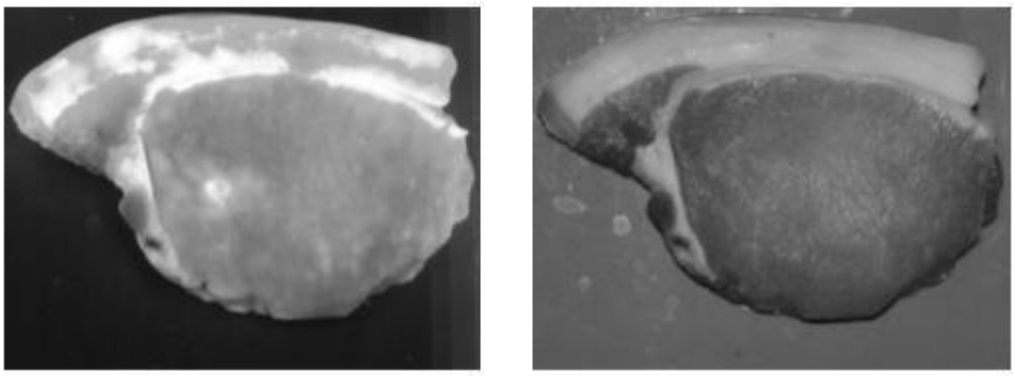

Figure 10 UV fluorescence and visible light images (a) UV fluorescence image (b) visible light image.

1503 Bld. A04, 3rd Software Park, Jimei, Xiamen, 361005, China
Tel: +86-592-6102588

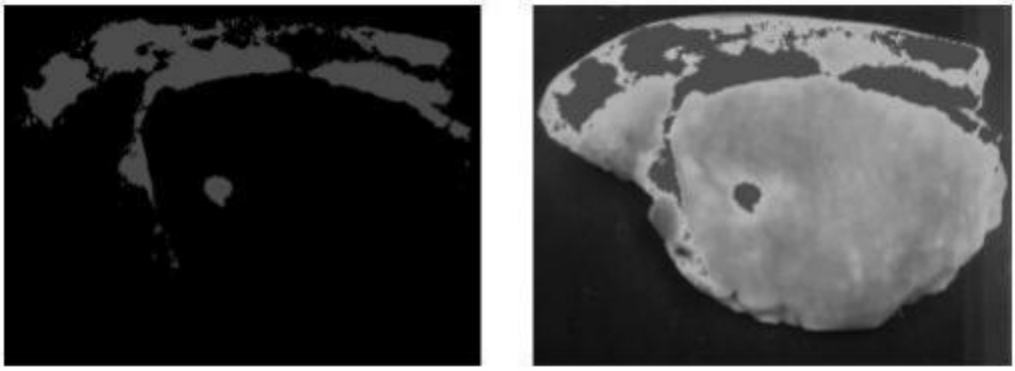

Figure 11 Image statistics of the area of the ultraviolet fluorescent area (a) the fluorescent area whose intensity exceeds a certain threshold (b) the fluorescent area is marked on the meat image.

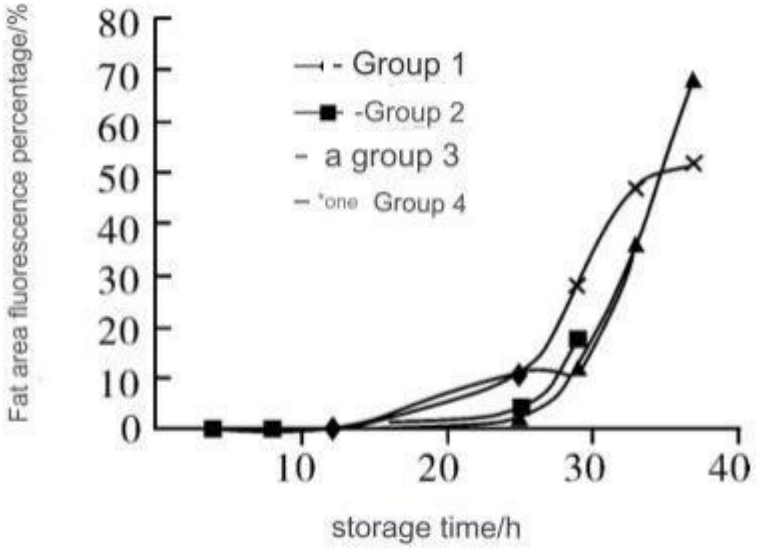

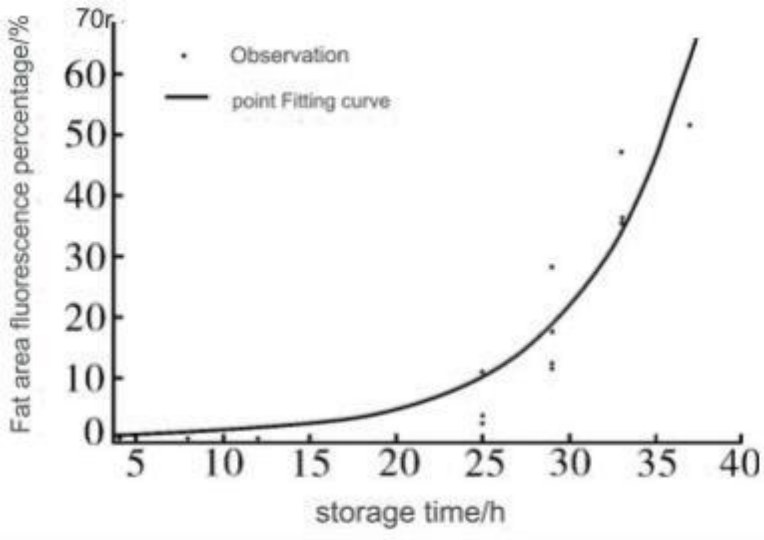

Figure 12 (a) Growth trend of fluorescence percentage in fat area (b)exponential growth curve fitting of fluorescence percentage in fat area with storage time.

1503 Bld. A04, 3rd Software Park, Jimei, Xiamen, 361005, China
Tel: +86-592-6102588

In conclusion:

1) The fluorescent product can be observed through the ultraviolet fluorescence image acquisition system, and it increases with the storage time.

2) The fluorescence image was segmented into regions, and the area of the fluorescence region increased with the increase of the storage time, especially in the area of the backfat and the skin of the meat, the monotonically increasing growth trend of the area of the fluorescence product was obvious.

3) The fluorescence area of the backfat and skin area showed an exponential growth law with the increase of storage time, and the coefficient of determination of the exponential function fitting R 2 = 0.9336, root mean square error RMSE = 5.186, indicating that it is feasible to conduct non-destructive testing of the storage time of packaged pork under certain storage conditions in specific parts based on fluorescence image acquisition.

4) The ultraviolet fluorescence in the muscle area grows weaker with the increase of storage time. In this experiment, the intensity level that the system can be used for predictive testing has not been reached. It is difficult to use the existing equipment to measure the storage time based on the ultraviolet fluorescence imaging of lean meat. predict.

5) There is a strong exponential correlation between the UV fluorescence percentage index and the storage time in the fat area in this observation. Since the production of ultraviolet fluorescent substances is related to microbial metabolism, the results of this experiment are in good agreement with the general law of microbial metabolic growth. Compared with the widely used microbial counting detection methods, ultraviolet fluorescence imaging detection methods are rapid and objective. As well as the advantages of non-contact with the measured object, it has broad application prospects in the rapid non-destructive testing of meat products.

4.5. Chlorophyll fluorescence imaging technology for monitoring wheat powdery mildew at seedling stage

Wheat powdery mildew is an airborne disease caused by the powdery mildew bacterium Blumeria graminis f.sp. The change of chlorophyll content varies with time and severity. Therefore, the degree of disease stress to plants can be understood through the change of chlorophyll content in leaves. But traditionally, the measurement of chlorophyll content mainly adopts ultraviolet spectrophotometry, which operates However, chlorophyll fluorescence technology can directly and quickly reflect the change of chlorophyll through chlorophyll fluorescence, which can be used as the basis for biological stress detection. In recent years, with the advancement of chlorophyll

1503 Bld. A04, 3rd Software Park, Jimei, Xiamen, 361005, China
Tel: +86-592-6102588

fluorescence measurement and imaging technology, especially the development of chlorophyll fluorescence imaging system Developed and proposed a way to obtain plant fluorescence from a macroscopic perspective. While obtaining fluorescence parameters, it also obtains fast, intuitive and accurate image information, which enables chlorophyll fluorescence imaging technology to overcome the shortcomings of limited point measurement of traditional fluorescence instruments. Therefore, it has gradually been widely used.

In terms of wheat powdery mildew, the use of laser-induced chlorophyll fluorescence (laser-induced chlorophyll fluorescence) to monitor the degree of wheat powdery mildew infection has been reported, but chlorophyll fluorescence imaging technology has rarely been reported in the monitoring of wheat powdery mildew.

In order to explore the feasibility of chlorophyll fluorescence imaging technology in the monitoring of wheat powdery mildew, in this study, isolated leaves, one-leaf-one-heart stage seedlings and two-leaf-one-heart stage seedlings of wheat seedlings inoculated with six different concentrations of powdery mildew conidia And the chlorophyll fluorescence imaging was measured at different periods after inoculation, and the relationship between the derived chlorophyll fluorescence parameters and the severity of the disease was analyzed. The results showed that the Fv/Fm of isolated wheat leaf segments or seedlings inoculated with different concentrations of powdery mildew conidia The image can reflect the infection degree of wheat powdery mildew to a certain extent. On the 3rd day after inoculation with wheat powdery mildew, the change of Fv/Fm value with the inoculation concentration is not obvious, but from the 5th day after inoculation, the Fv/Fm The value decreased with the increase of inoculation concentration, and the Fv/Fm value of uninoculated wheat seedlings or detached leaves was significantly higher than that of inoculated treatment, and the Fv/Fm value of the treatment with the highest inoculation concentration (5 mg/mL) was significantly lower Other inoculation treatments at the same period. The correlation analysis between the severity of wheat powdery mildew and chlorophyll fluorescence parameters showed that Fv/Fm and Chlidx were extremely significantly negatively correlated with the severity of the disease. On this basis, the wheat The disease severity estimation models based on parameters Fv/Fm or Chlidx for detached leaves, seedlings with one leaf and one heart, and seedlings with two leaves and one heart. Comparing the fitting effects of the models, it was found that the disease estimation model based on Fv/Fm or Chlidx RMSE or R2 are relatively close, so the chlorophyll fluorescence parameter Fv/Fm or Chlidx is feasible to estimate the occurrence degree of wheat powdery mildew at seedling stage.

1503 Bld. A04, 3rd Software Park, Jimei, Xiamen, 361005, China
Tel: +86-592-6102588

Chlorophyll fluorescence imaging technology is an ideal method for rapid and non-invasive research on photosynthetic physiology of plants under stress. Existing studies have shown that disease stress can reduce the Fv/Fm value of chlorophyll fluorescence parameters in cotton, grapevine, tobacco and other plants. In this study, the color distribution of Fv/Fm images of wheat leaves infected by powdery mildew will change with the aggravation of disease infestation, and the Fv/Fm value is significantly lower than that of uninfected leaves, which indicates that the use of chlorophyll Fluorescent image parameters to monitor the severity of wheat powdery mildew are feasible.

There was a very significant negative correlation between the severity of wheat powdery mildew and the chlorophyll fluorescence parameters Fv/Fm and Chlidx, because the infection of powdery mildew would cause the decrease of chlorophyll content of wheat leaves, thus leading to the decrease of Chlidx.

1503 Bld. A04, 3rd Software Park, Jimei, Xiamen, 361005, China
Tel: +86-592-6102588

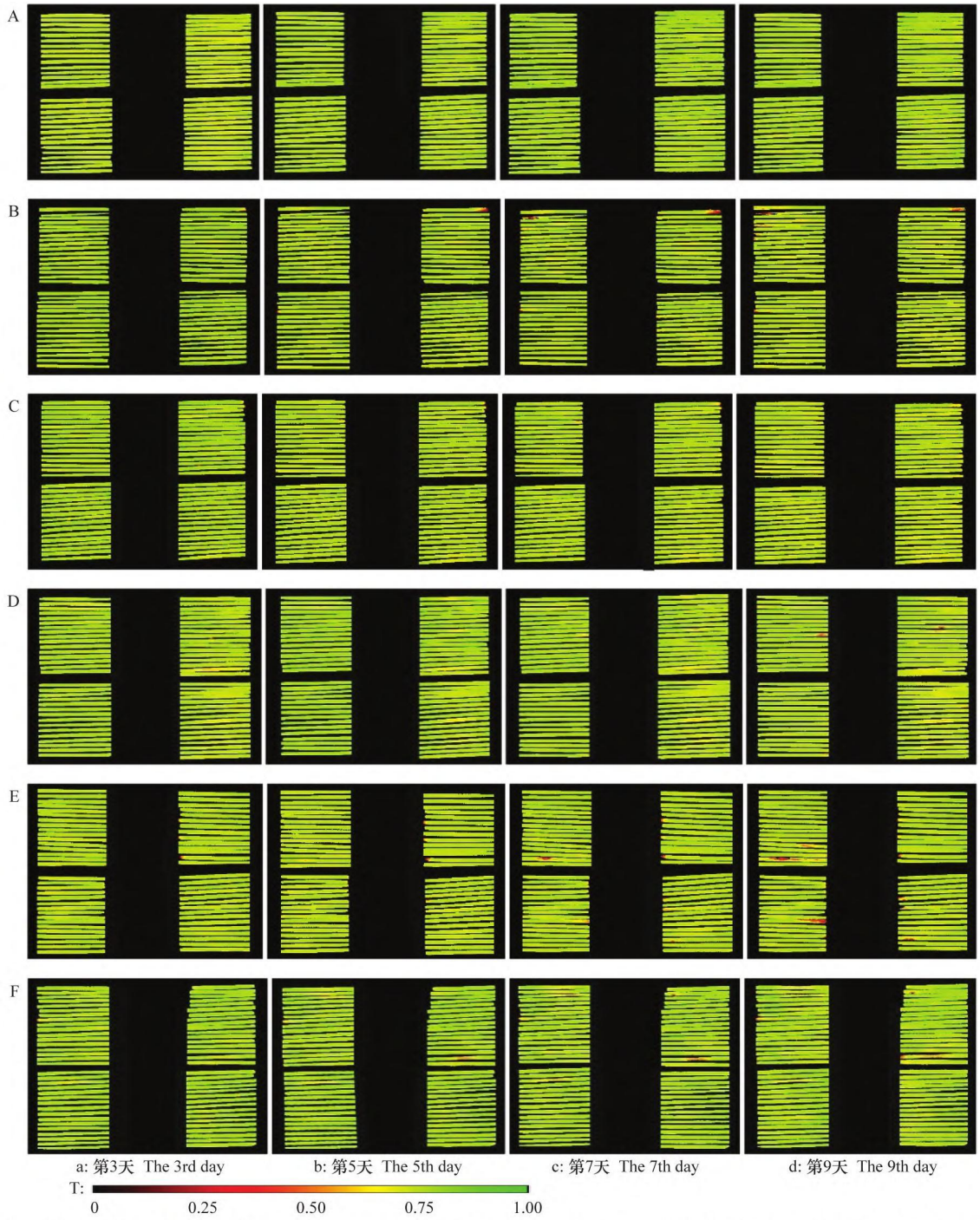

A~F: 离体叶段接种的白粉病菌分生孢子浓度为1、2、3、4、5 mg/mL和0 mg/mL。a~d: 离体叶段接种分生孢子后第3、5、7天和第9天获取的Fv/Fm图像; T: 假色标

A- F: The inoculation concentration of Bgt spores in detached wheat leaf segments was 1, 2, 3, 4, 5 mg/mL and 0 mg/mL, respectively. a-d: Fv/Fm images at the 3rd-, 5th-, 7th- and 9th- day after inoculation of Bgt spores, respectively. T: False color mark

Figure 13 Fv/Fm images of isolated wheat leaf segments inoculated with different concentrations of powdery mildew.

4.6. High-throughput counting of soybean cyst nematode browning cysts

Soybean cyst nematode (Heterodera glycines Ichinohe) disease is the most serious soil-borne disease in soybean production. Due to the wide distribution range of soybean cyst nematodes, long survival time of dormant bodies, multiple transmission routes, and

1503 Bld. A04, 3rd Software Park, Jimei, Xiamen, 361005, China
Tel: +86-592-6102588

rich population diversity, it is extremely difficult to control in soybean production. It generally causes 5% to 10% yield loss every year, and yields are reduced in severe areas. More than 30%, even the cyst nematodes of grainless soybeans have three insect states: eggs, larvae and adults. After mating, the body of the mature female worm is filled with eggs, and the body of the worm continues to expand. Most of the worms break through the epidermis and are exposed to the outside of the root, taking a spherical shape, while the head and neck remain within the root. After the death of the female, the body wall thickens and hardens, and the color gradually changes from white or light yellow to dark brown, which is called a cyst. We call white or light yellow cysts "fresh cysts" and brown cysts "brown cysts". During the peak cyst development period, the number of cysts on soybean roots is an important indicator for evaluating the incidence of soybean cyst nematode disease. Therefore, cyst counting is an indispensable link in the research on soybean cyst nematode resistance.

Traditional cyst counting involves distinguishing cysts with the naked eye or a dissecting microscope, and manually counting the number of cysts. This method is time-consuming and labor-intensive and is not suitable for batch statistics. In 2006, Lu et al. established a cyst counting method based on a fluorescence imaging system. This method uses halogen light as the excitation light source, obtains excitation light and emission light of appropriate wavelengths through filters, and increases the distance between fresh cysts and soybean roots. The difference in intensity of the emitted fluorescence can be used to obtain high-contrast, clear photos, which can then be counted manually. In 2010, Brown et al. improved this method and used imaging analysis software to realize automatic counting, enables high-throughput greenhouse resistance phenotyping. However, because halogen or xenon is used as the excitation light source, the energy is relatively low, so previous methods are mainly used for counting fresh cysts. Experiments have found that if the plant roots are dug out of the soil and the cysts are not washed out in time, or if the cysts are washed out and stored improperly, cysts will all turn brown. When the cysts brown, the fluorescence signal becomes weak, and it is difficult to obtain clear image results using the above method. This defect limits the use of this technology.

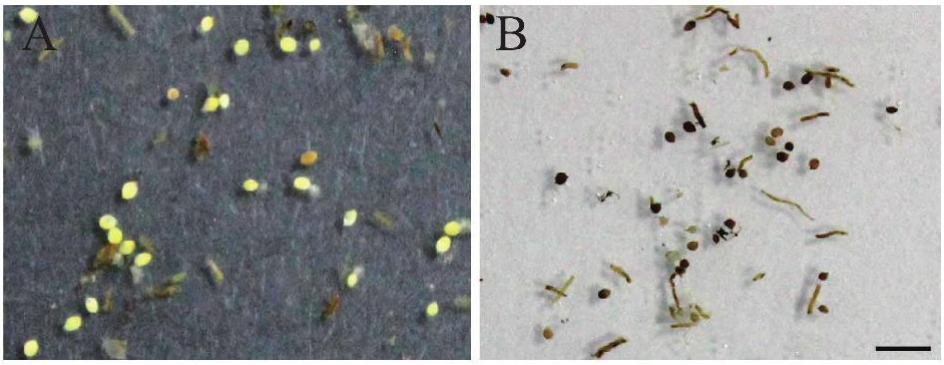

Figure 14 Comparison of fresh cysts (A) and browned cysts (B).

Using laser light source instead of halogen or xenon improves the excitation light source of the fluorescence imaging system, effectively increasing the energy of the excitation light, so that browned cysts can also obtain strong fluorescence signals and obtain high-contrast, clear photos. At the same time, the imaging analysis software can realize automatic counting. This technology relaxes the time limit of the original method for counting cysts, making it possible to conduct large-scale field resistance screening that could not be completed in batches. It is of great significance to the study of cyst nematodes.

In order to improve the problem that the excitation light energy of ordinary fluorescence imaging systems is low, the fluorescence excited by browned cysts is weakened, it is

1503 Bld. A04, 3rd Software Park, Jimei, Xiamen, 361005, China
Tel: +86-592-6102588

difficult to image clearly, and the counting effect is poor, this study switched to laser as the excitation light source, with an excitation wavelength of 470nm and 535nm. Under the combination of emission wavelengths or the combination of 532nm excitation wavelength and 620nm emission wavelength, high contrast and clear pictures of browned cysts can be obtained. With the use of automatic counting software, cysts can be counted accurately and efficiently.

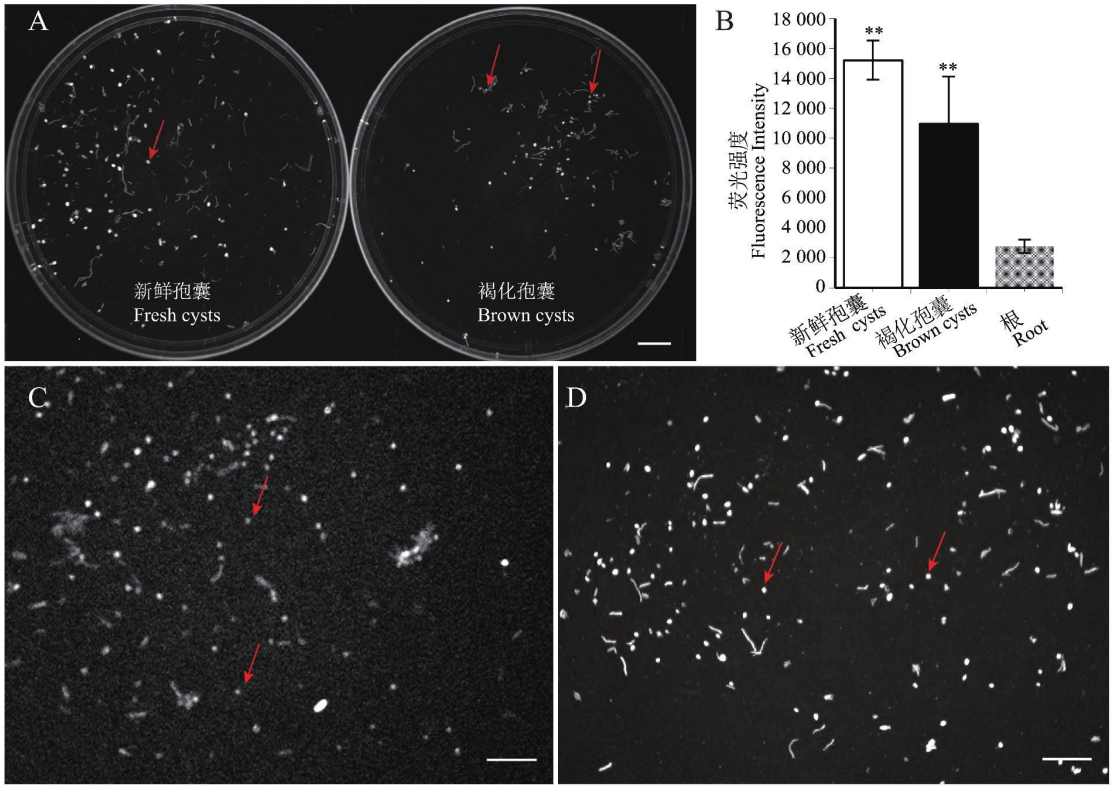

Figure 15 Comparison of fluorescence imaging between laser excitation and xenon lamp excitation Note: A: Comparison of fluorescence imaging between fresh cysts and browned cysts; B: Histogram of fluorescence intensity data of fresh cysts, browned cysts, and roots. n =30, **: p <0. 01(Student's t-test). C and D are comparisons of fluorescence imaging of browned cysts using xenon light source and laser light source as excitation light sources respectively. Arrows indicate cysts. All tests are completed under the condition of 532nm excitation light, 620nm emission light, and exposure time of 10s. Ruler=5mm.

Select 470nm or 532nm wavelength laser as the excitation light, and match different emission light wavelengths to take pictures. It was found that 470nm excitation light combined with 535nm emission light, and 532nm excitation light combined with 620nm emission light can achieve the best photographing effect. Then we explored the exposure time and found that 470nm excitation light combined with 535nm emission light can achieve the best shooting effect when the exposure time is 6s; 532nm excitation light with 620nm emitted light can achieve the best shooting results when the exposure time is 15s.

1503 Bld. A04, 3rd Software Park, Jimei, Xiamen, 361005, China
Tel: +86-592-6102588

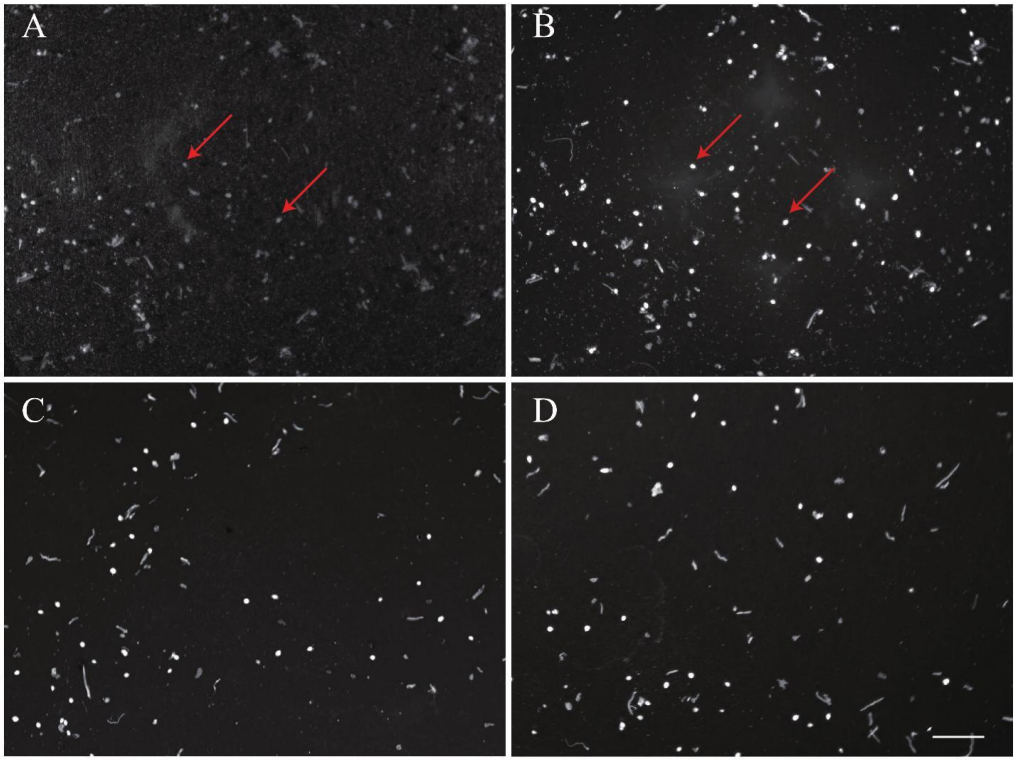

Figure 16 Photos of browned cysts taken under optimized conditions. Notes : A: bright field, natural light and 0.3s exposure time; B: dark field, 532nm excitation light, 620nm emission light, exposure time 15s. Arrows indicate cysts that correspond to each other in Figure 3A and Figure 3B. C: 470nm excitation light, 535nm emission light, exposure time 6s; D: 532nm excitation light, 620nm emission light, exposure time 15s. The scale is 5mm.

4.7. Research on bee pollen balls and single bee pollen

While keeping the filter wavelength at 550 nm, the system performed transmission spectrum imaging and fluorescence spectrum imaging of bee pollen clumps and single bee pollen, respectively. The results are shown in the figure. In the transmission spectrum image using LED illumination, the shape of the pollen appears as an irregular ball with a central cavity. However, the central cavity cannot be observed in the laser-excited fluorescence spectrum image. In fact, both spectral images were taken by the same optical imaging system, and their optical resolutions should be consistent. That is, the structures that can be observed in the transmission spectrum image should also be able to be observed in the fluorescence spectrum image. arrive. Therefore, there must be a reason for the different structures of bee pollen in the two images.

1503 Bld. A04, 3rd Software Park, Jimei, Xiamen, 361005, China
Tel: +86-592-6102588

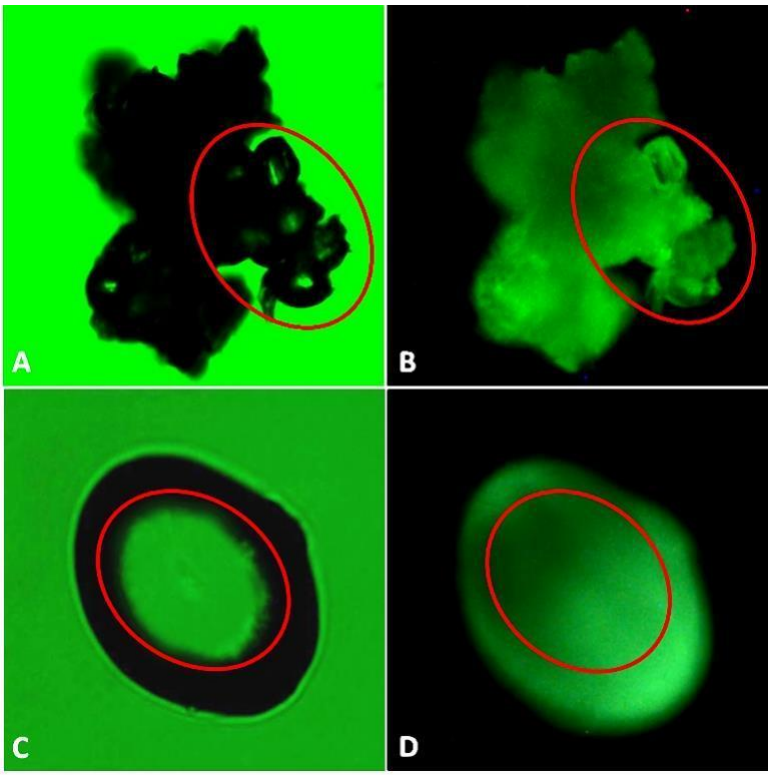

Figure 17 Bee pollen cluster transmission spectrum imaging (A) fluorescence spectrum imaging (B) single bee pollen transmission spectrum imaging (C) fluorescence spectrum imaging (D) All images were taken at a filtered wavelength of 550 nm.

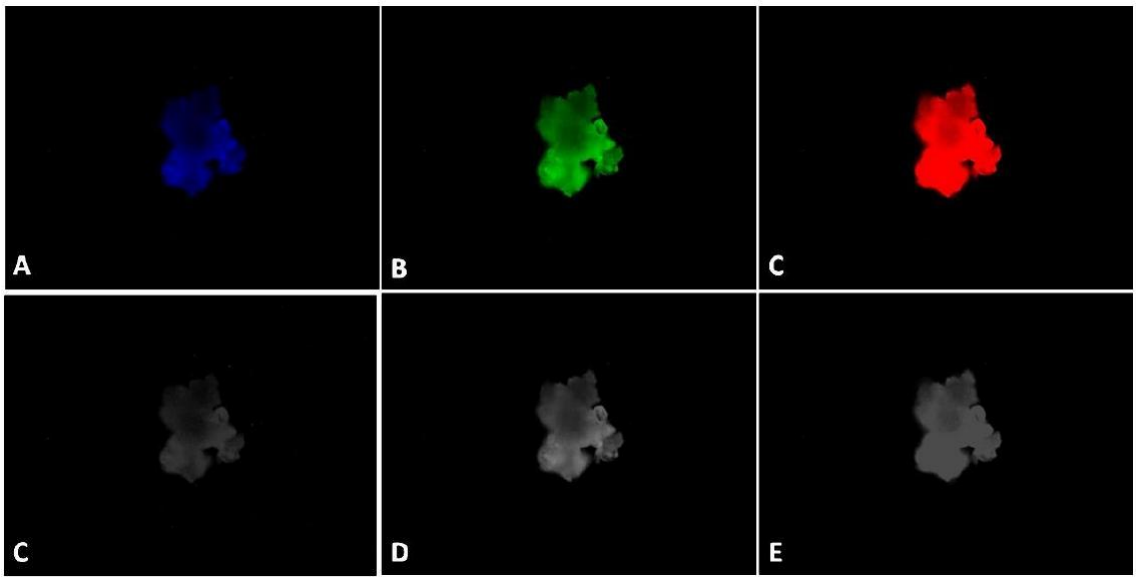

Figure 18 Color images and grayscale images of the fluorescence spectra of pollen masses at 480 nm (A, C), 535 nm (B, D), and 590 nm (C, E) (410nm laser excitation).

1503 Bld. A04, 3rd Software Park, Jimei, Xiamen, 361005, China
Tel: +86-592-6102588

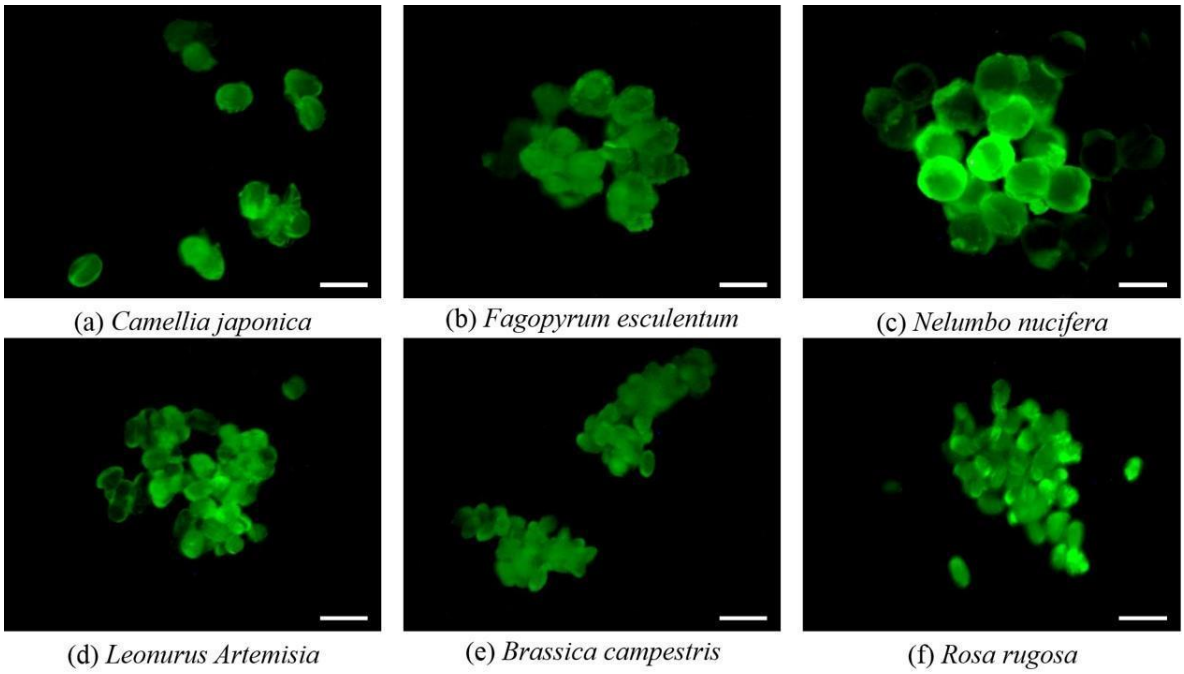

Figure 19 Fluorescence images of bee pollen cells: (a) C. japonica, (b) F. esculentum, (c) N. nucifera, (d) L.artemisia, (e) B. campestris and (f) R. rugosa. The 550 nm band image is given because the fluorescence intensity is strong in this band, and the scale bar in the figure is 50 μm.

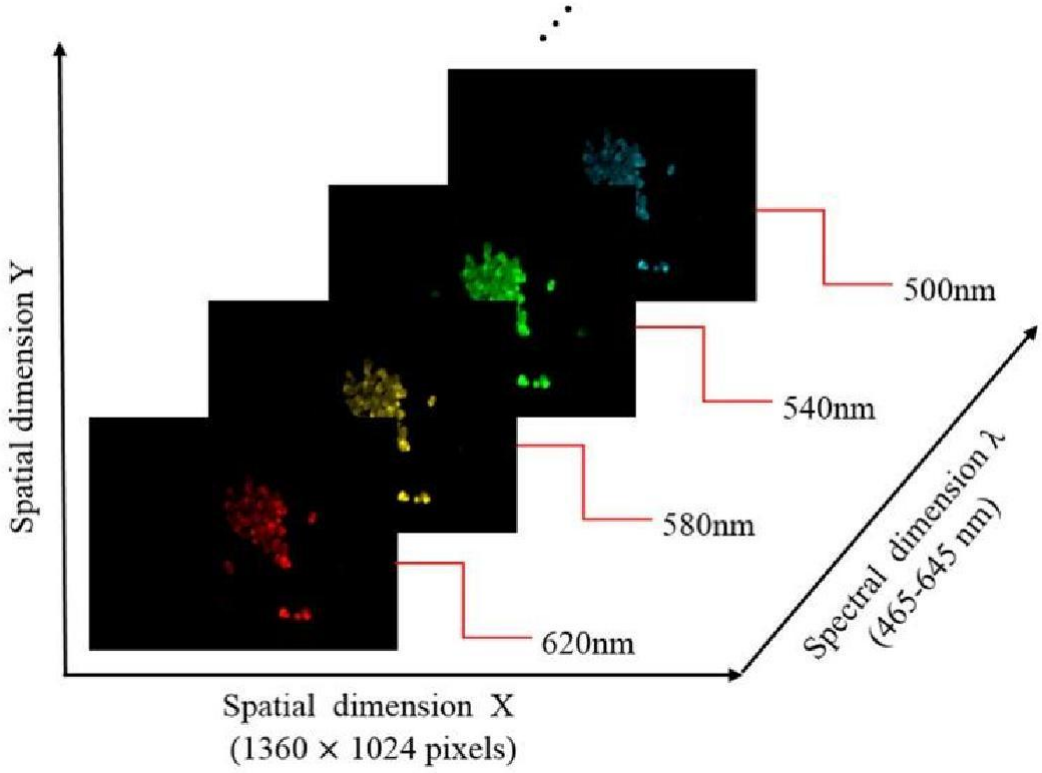

Figure 20 R. rugosa pollen cell hyperspectral data set.

Bee pollen cell fluorescence spectral information is stored in a hyperspectral data cube. As shown in Figure 3.2, the hyperspectral microscopy data set contains both spectral information and image information, thus ensuring the theoretical feasibility of identifying pollen types on images. Each pixel in the image has n dimensions.

1503 Bld. A04, 3rd Software Park, Jimei, Xiamen, 361005, China
Tel: +86-592-6102588

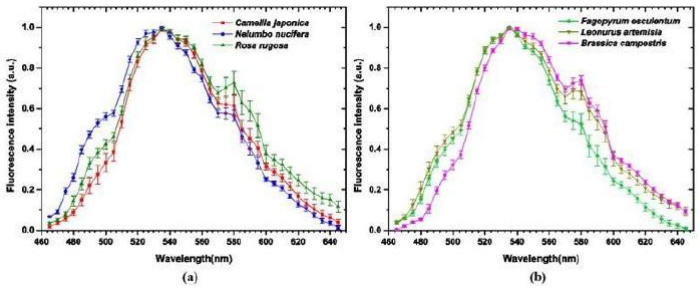

Figure 21 Normalized fluorescence spectral curves of 6 species of bee pollen. (a) C. japonica, N. nucifera and R. rugosa. (b) F. esculentum, L. artemisia and B. campestris Each curve represents the average result of 100 pixels in the ROI and is accompanied by the standard deviation.

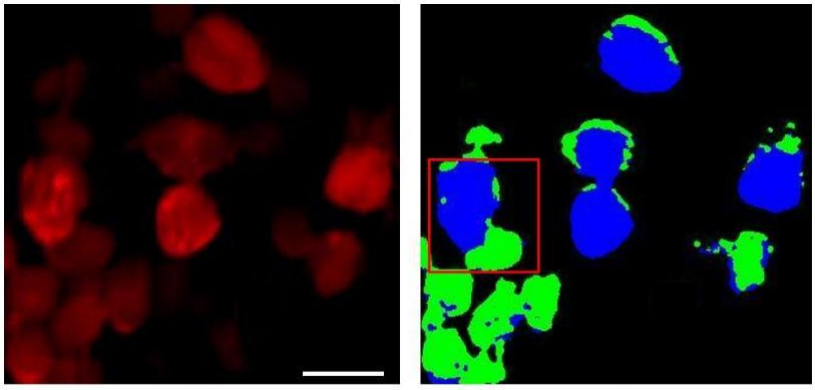

Figure 22 Another case of mixed bee pollen identification: (a) The 645 nm band contains 2 types of bee pollen cells with similar morphology sample. (b) Pseudocolor image after median filtering (L. artemisia is marked in blue, R. rugosa is marked in green, scale bars are 20μm).

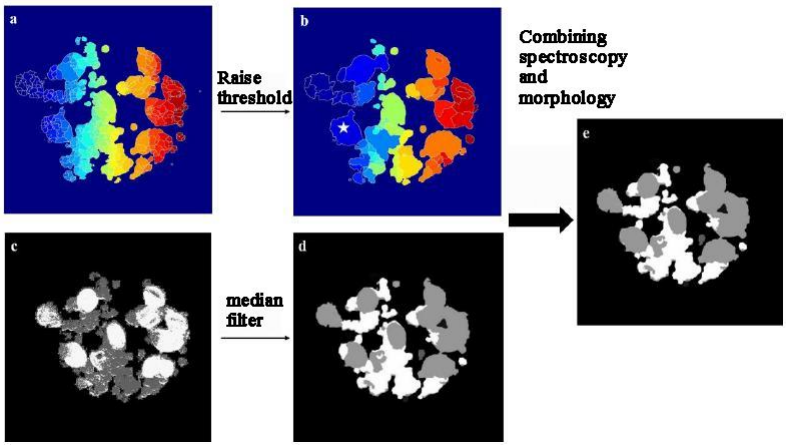

Figure 23 Improvements to the pollen cell binding morphology in Figure 3.5. (a) The segmentation result of the watershed algorithm. The small value of the gradient function threshold leads to over-segmentation. (b) Segmentation results of the watershed method modified by increasing the threshold (c) Spectral classification results (d) Spectral classification image after median filtering (d) The final optimized classification map generated by combining morphology and spectrum, marked star-shaped area results improved. Note: The watershed transformation process uses switching operations and threshold segmentation to remove isolated and small pollen pixels with pixel values.

4.8. Research on early diagnosis methods of gastric cancer

Early and timely diagnosis of gastric cancer (GC) can effectively reduce the incidence and mortality of gastric cancer. Current clinical methods for early diagnosis of gastric

1503 Bld. A04, 3rd Software Park, Jimei, Xiamen, 361005, China
Tel: +86-592-6102588

cancer still have shortcomings such as strong subjectivity, cumbersome testing procedures, time-consuming, and easy missed diagnosis. Therefore, exploring an objective, rapid and accurate early diagnosis method for gastric cancer has important clinical application value and scientific research significance.

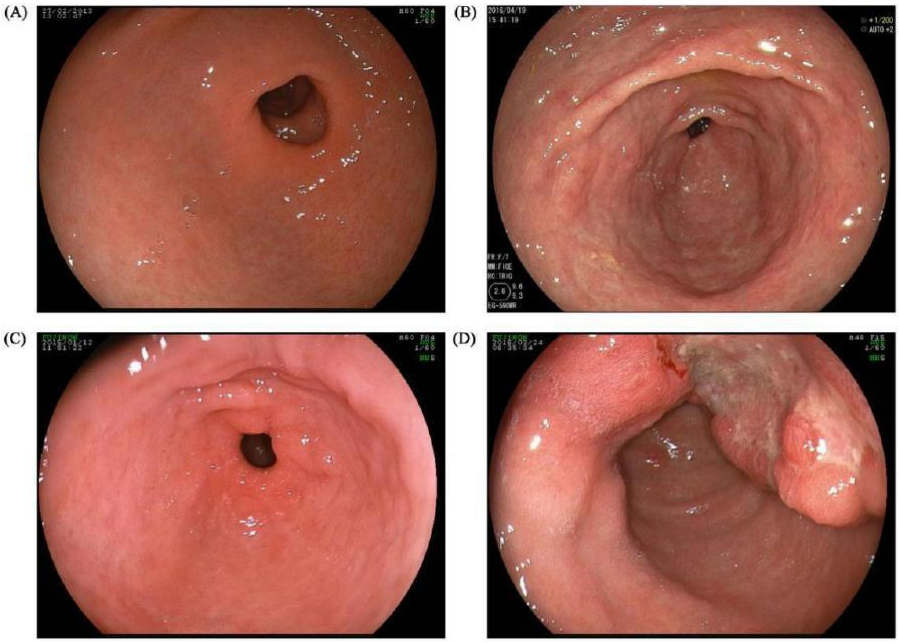

Figure 24 Endoscopic images: (A) Normal tissue; (B) Moderate atrophy; (C) Severe atrophy with intestinal metaplasia; (D) Gastric mucinous adenocarcinoma.

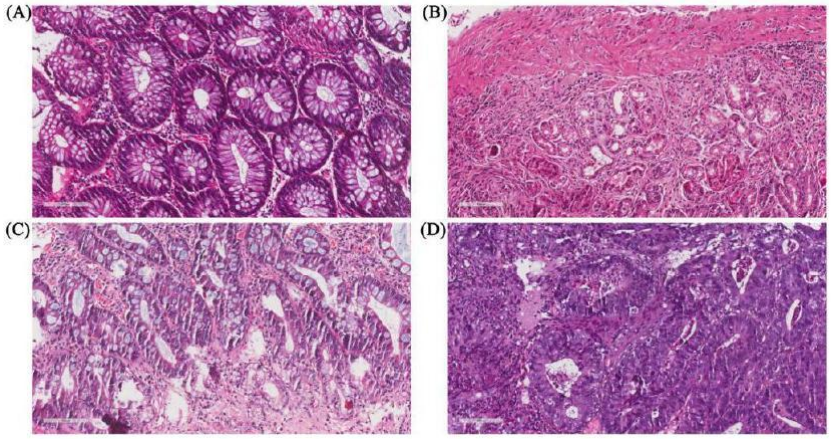

Figure 25 Standard pathological type images: (A) Normal; (B) Atrophic gastritis; (C) Atrophy with intestinal metaplasia; (D) Gastric cancer.

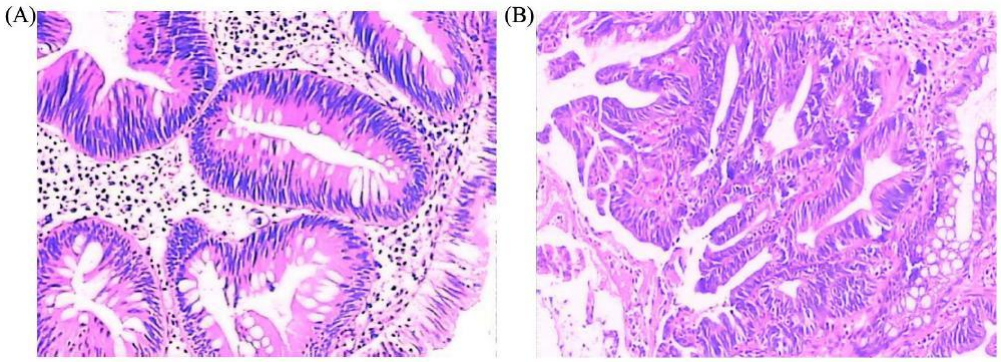

1503 Bld. A04, 3rd Software Park, Jimei, Xiamen, 361005, China
Tel: +86-592-6102588

Figure 26 Histological and pathological pictures of precancerous lesions: (A) Dysplasia; (B) Intraepithelial neoplasia.

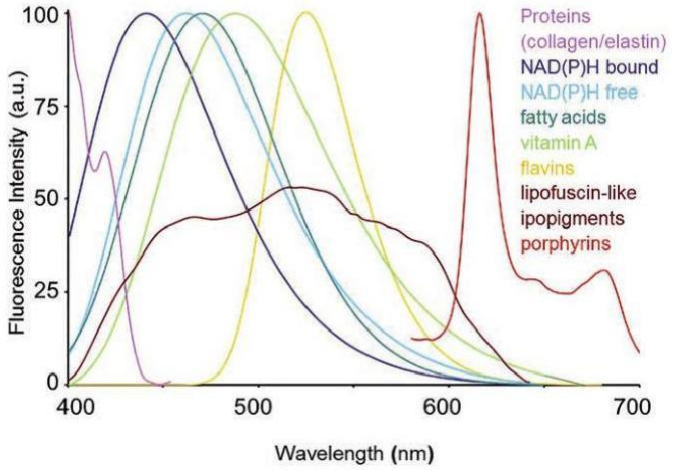

Figure 27 Typical spectra of autofluorescence of human tissue components.

Fluorescence hyperspectral imaging technology is used to collect fluorescence spectrum images (450-680 nm) of gastric mucosal tissue samples. The image is binarized to obtain the area of interest, and the fluorescence spectrum of 100 pixels is randomly extracted. Analyzing the differences and changes in fluorescence components among the non-precancerous lesion group, precancerous lesion group and gastric cancer group through fluorescence spectrum; then, a model for early diagnosis of gastric cancer (including non-precancerous lesion group, precancerous lesion group and gastric cancer group) was established using traditional machine learning methods combined with spectral features ; Secondly, the space-spectrum joint classification method is used to fuse spectral and spatial information, and a gastric cancer early diagnosis model is established by manually extracting the "space + spectrum" features after space-spectrum union and integrated learning, and compared with integrated learning combined with spectral feature modeling; Finally, the deep learning method is used to automatically identify and extract the "space + spectrum" features after the combination of space and spectrum to establish an early diagnosis model for gastric cancer.

Normal, atrophic gastritis, intestinal metaplasia and gastric cancer were divided into three groups: non-precancerous lesion group, precancerous lesion group (atrophic gastritis, intestinal metaplasia) and gastric cancer group. Figure 28[(A)-(C)] shows the Gaussian fitting spectra of the non-precancerous lesion group, precancerous lesion group and gastric cancer group. The Gaussian fitting spectrum of non-precancerous lesions group and precancerous lesions group can extracted eight characteristic peaks: pyridoxal phosphate "Schiff" base (496 nm, 515 nm), nuclide/FAD (529 nm), phospholipid (546 nm, 556 nm), blood porphyrin (634 nm, 675 nm) and unknown fluorescence emission peaks in 597 nm bands. The gastric cancer group has one less characteristic peak than the non-precancerous group and precancerous lesion group, which is the phospholipid fluorescence emission peak at 546 nm. Figure 28(D) shows the average spectra of the non-precancerous lesion group, precancerous lesion group and gastric cancer group.

1503 Bld. A04, 3rd Software Park, Jimei, Xiamen, 361005, China
Tel: +86-592-6102588

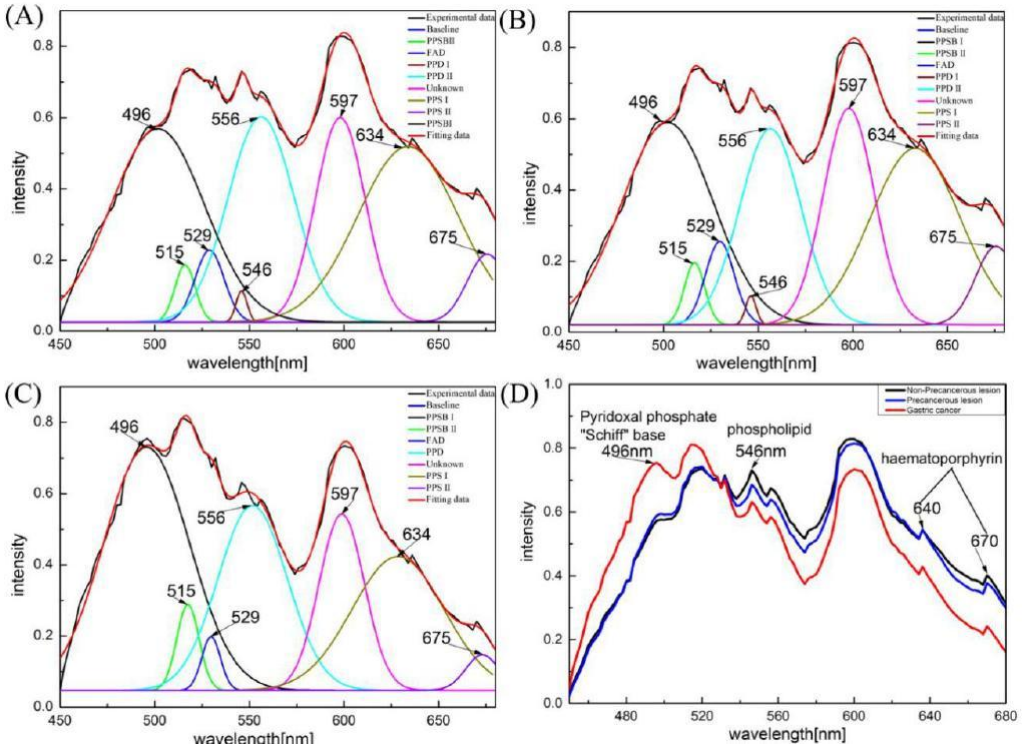

Figure 28 Original fluorescence spectrum (black) and Gaussian fitting spectrum (red): (A) Non-precancerous lesion group; (B) Precancerous lesion group; (C) Gastric cancer group; (D) The average spectrum of each group.

It can be seen in Figure 28(D) that the fluorescence spectra of the gastric cancer group and the non-gastric cancer group are significantly different, mainly manifested in: 496 nm corresponds to the fluorescence emitted by pyridoxal phosphate "Schiff" base in vitamin B6 compounds in organisms, has a strong fluorescence peak at 496 nm in gastric cancer tissue, which may be caused by abnormal metabolism of the pyridoxal phosphate "Schiff" base concentration in the malignant tissue; 546 nm corresponds to the fluorescence emitted by phospholipids in biological lipids, and the fluorescence emission peak intensity is the non-precancerous lesion group > precancerous lesion group > gastric cancer group, may be caused by abnormal phospholipid metabolism in tissues or cells with the development of malignant transformation; 640 nm and 670 nm correspond to the fluorescence emitted by hematoporphyrin IX in organisms. The fluorescence intensity of the gastric cancer group is lower than that of the non-gastric cancer group, while the fluorescence spectrum of the non-precancerous lesion group is different from that of the precancerous lesion group. The differences are small and almost overlap. Porphyrin-related biomarkers are intermediates in the heme biosynthetic pathway. This difference between the gastric cancer group and the non-gastric cancer group may be due to the fact that heme metabolism in cancerous tissues is more intense than in normal tissues. These differences indicate changes in fluorophore composition in tissues during tumor transformation. These endogenous fluorescent substances can be used as spectral biomarkers to distinguish non-precancerous lesions, precancerous lesions and gastric cancer.

1503 Bld. A04, 3rd Software Park, Jimei, Xiamen, 361005, China
Tel: +86-592-6102588

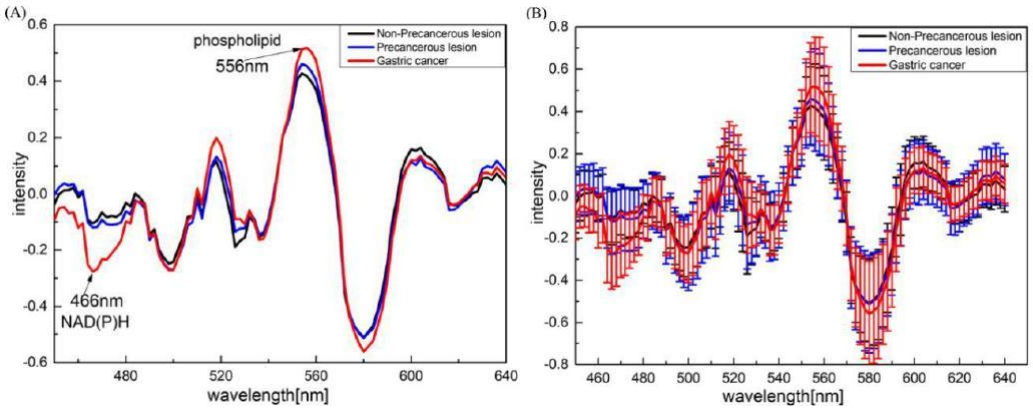

Figure 29 Second-order derivative spectra of the non-precancerous lesion group, precancerous lesion group and gastric cancer group: (A) Second-order derivative average spectrum; (B) Second-order derivative spectrum with error bars.

Fluorescence hyperspectral imaging can obtain the fluorescence intensity in two spatial dimensions and one wavelength dimension on the surface of the sample to be measured, which is called a "Hypercube" (Figure 30(B)). Therefore, the fluorescence spectrum image can be understood as the extension of the fluorescence spectrum image in the wavelength dimension, that is, collecting sample images at multiple fluorescence emission wavelengths; it can also be It is regarded as the extension of the fluorescence spectrum in the dimension of the plane to be measured, and each pixel in the image scans a fluorescence spectrum. Fluorescence hyperspectral imaging technology is superior to traditional monochrome, RGB color images and fluorescence spectrum methods. Because fluorescence hyperspectral images contain more information than traditional monochromatic imaging, RGB imaging, and fluorescence spectroscopy, and spatial relationships between different spectra in a neighborhood can be exploited, which enables more sophisticated "spectral + spatial" models to be used to accurately segment and It becomes possible to classify images. Therefore, fluorescence hyperspectral imaging technology can find broader application scenarios in the early diagnosis of diseases and cancer.

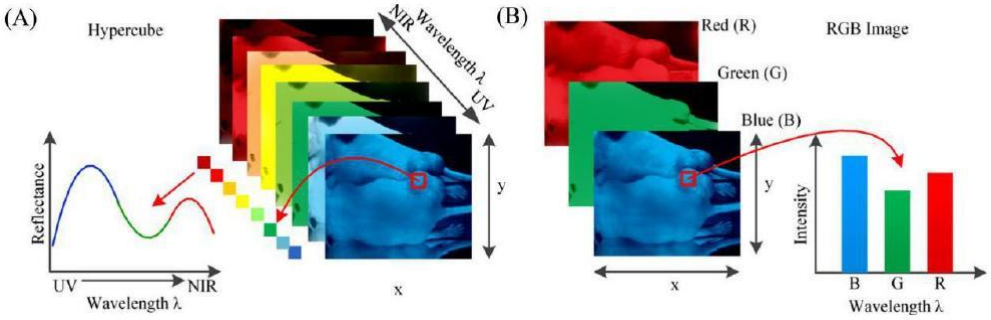

Figure 30 (A)Hypercube of spectral image; (B) RGB color image.

1503 Bld. A04, 3rd Software Park, Jimei, Xiamen, 361005, China
Tel: +86-592-6102588

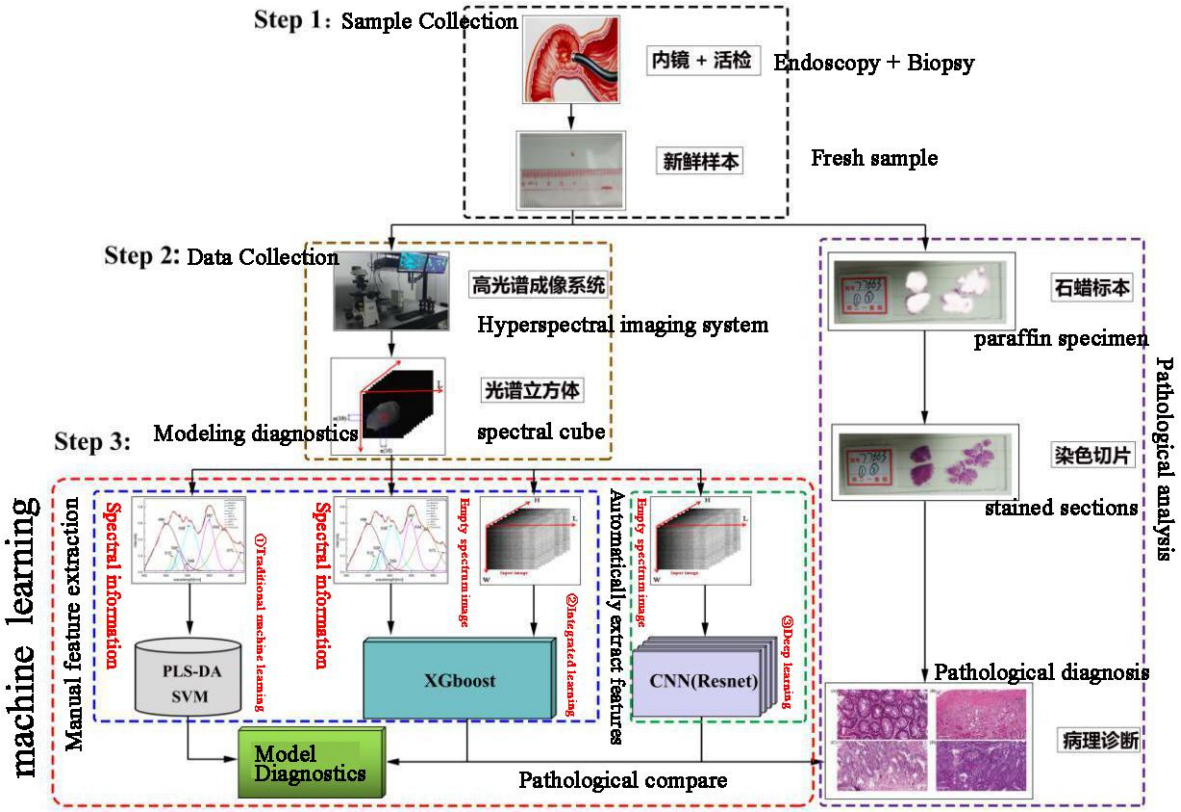

Figure 31 Research technology roadmap.

In gastric cancer tissue, the fluorescence peak at 496 nm is strong, and the fluorescence peaks at 640 nm and 670 nm are weak, which may be caused by abnormal metabolism of pyridoxal phosphate "Schiff" base concentration and blood porphyrin IX concentration in malignant tissue; 546nm corresponding to the fluorescence emitted by phospholipids in biological lipids, the fluorescence emission peak intensity is non-precancerous group > precancerous lesion group > gastric cancer group. Abnormal phospholipid metabolism reflects the severity of lesion development; these differences indicate changes in fluorophore composition in tissues during tumor transformation. These endogenous fluorescent substances can be used as spectral biomarkers to distinguish non-precancerous lesions, precancerous lesions and gastric cancer. However, due to the great influence of spatial distribution differences of tissue components, individual differences and instrument noise, the fluorescence spectrum overlap is serious, which may easily lead to misjudgment. The PLS-DA results showed that the accuracy, specificity, and sensitivity of the non-precancerous lesion group and the precancerous lesion group were 81.2%, 79.8%, and 86.3% respectively; the accuracy, specificity, and sensitivity of the precancerous lesion group and gastric cancer group were 87.5%, 87.5%, and 89.9% respectively; the accuracy, specificity, and sensitivity of the precancerous lesion group and gastric cancer group were 82.1%, 95.3%, and 76.4% respectively. The SVM results showed that the accuracy, specificity, and sensitivity of the non-precancerous lesion group and the precancerous lesion group were 92.8%, 94.0%, and 90.9% respectively; the accuracy, specificity, and sensitivity of the non-precancerous lesion group and the gastric cancer group were 95.6%, 96.5%, and 94.3% respectively; the accuracy, specificity, and sensitivity of the non-precancerous lesion group and gastric cancer group were 95.6%, 96.5%, and 94.3% respectively; the accuracy, specificity, and sensitivity of the precancerous lesion group and gastric cancer group were 94.9%, 94.7%, and 95.8% respectively. The accuracy rate of the early diagnosis models for gastric cancer established by SVM is above 92%, and the effect

1503 Bld. A04, 3rd Software Park, Jimei, Xiamen, 361005, China
Tel: +86-592-6102588

is significantly better than PLS-DA.

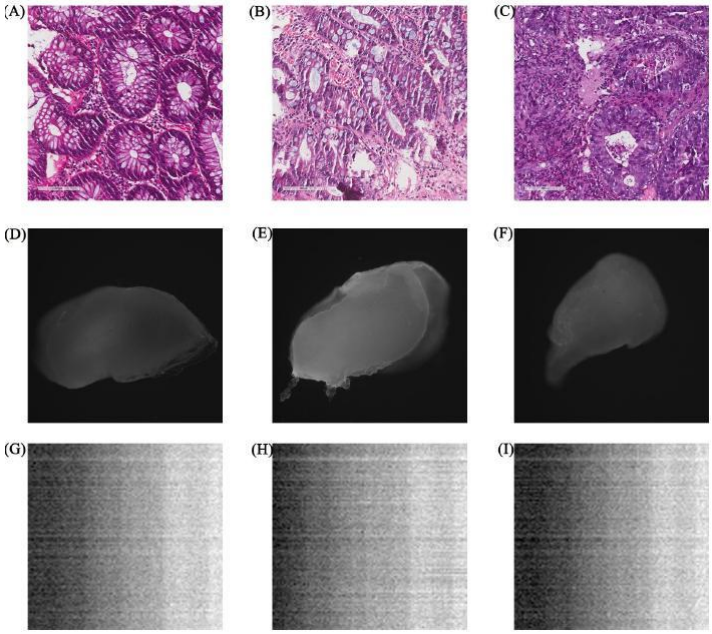

Figure 32 Images of non-precancerous lesions, precancerous lesions and gastric cancer: (A)-(C) Histopathological images; (D)-(F) Original fluorescence images; (G)-(I) Images after spatial spectrum combination.

The early identification model of gastric cancer constructed through fluorescence hyperspectral imaging combined with machine learning can provide better reference information for early diagnosis of gastric cancer, and modeling through deep learning combined with space-spectrum joint classification method can effectively improve the diagnostic accuracy of early gastric cancer, which is expected to Becomes a new method for early diagnosis of gastric cancer.

4.9. Microalgae identification and pigment information based on fluorescence hyperspectral imaging system

The fluorescent material components of Anabaena algae are phycocyanin, β-carotene and a small amount of chlorophyll a. The measured fluorescence spectrum shows that Anabaena algae has double fluorescence peaks, which are 660nm and 675nm respectively, and there is also a shoulder peak at 712nm. This shows that there are PC and APC corresponds to the peak at 660nm, while the peaks at 675nm and 712nm cannot be inferred as to what substance they are, and further analysis is required. Microcystis aeruginosa produces red fluorescence when excited by 462nm light. The hyperspectral reconstructed grayscale image is overlaid with a layer of spectral information color to obtain a pseudo-color Figure 33(c) the red part in the corresponding fluorescence peak is 660nm, indicating the fluorescence of phycocyanin; the very small yellow part corresponds to the position of β-carotene and phyllin a. Comparing Figure 33 (a) and Figure 33(c), the spectral distribution pattern of Microcystis aeruginosa in the fusion diagram is regular. The spectral distribution of Anabaena algae is obviously different from Microcystis aeruginosa. Although the two types of microalgae have similar fluorescence spectra, but the hyperspectral chart has the advantage of integrating the spectra into one, which can clearly determine the difference between the two microalgae. In the experimentally measured fluorescence spectrum of Chlorella, only one fluorescence peak was observed at 680nm, which corresponds to the theoretical peak of chlorophyll a around 670nm. However, carotenoids can be vaguely observed in the range of 450-520nm, and their spectral intensity is very weak, about 1/400 of chlorophyll a . Chlorella is shown to be rich in chlorophyll a

1503 Bld. A04, 3rd Software Park, Jimei, Xiamen, 361005, China
Tel: +86-592-6102588

and a small amount of carotenoids.

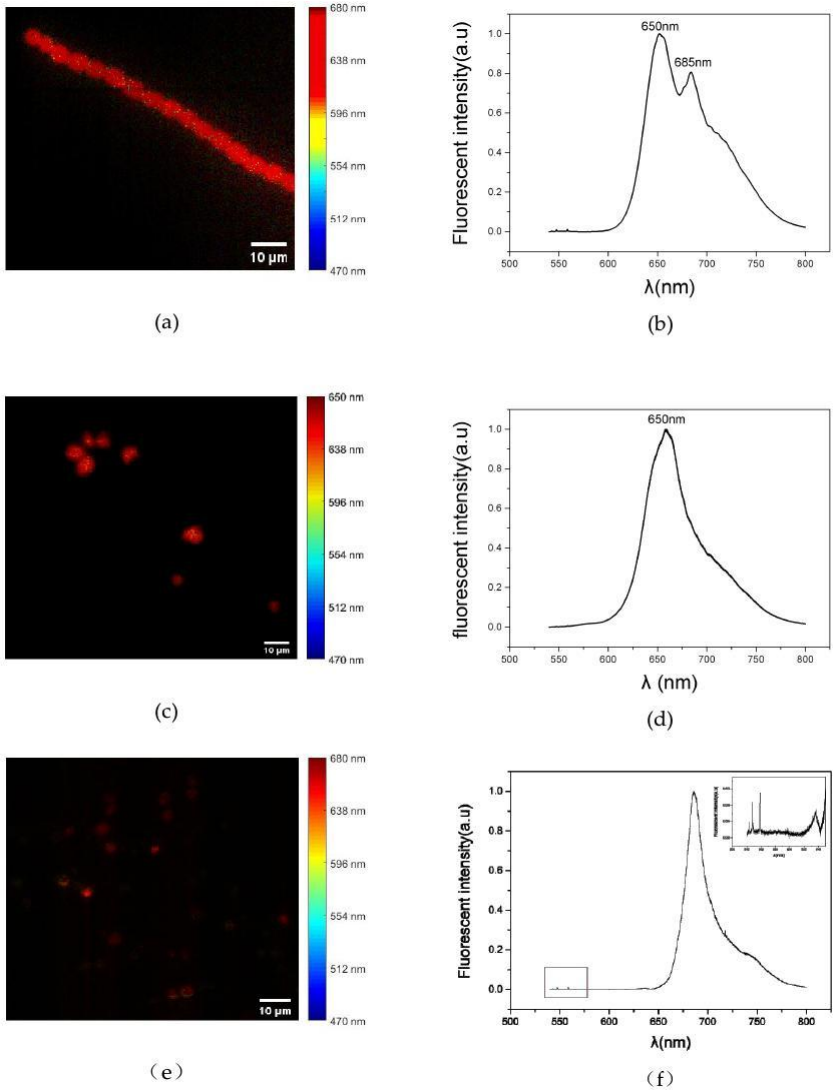

Figure 33 Hyperspectral fusion chart and its pure component spectrum (a) Spectral fusion chart of Anabaena blooms (b) Fluorescence spectrum chart of Anabaena blooms (c) Spectral fusion chart of Microcystis aeruginosa (d) Fluorescence spectrum of Microcystis aeruginosa (e) Spectral fusion chart of Chlorella (f) Fluorescence spectrum of Chlorella.

1503 Bld. A04, 3rd Software Park, Jimei, Xiamen, 361005, China
Tel: +86-592-6102588

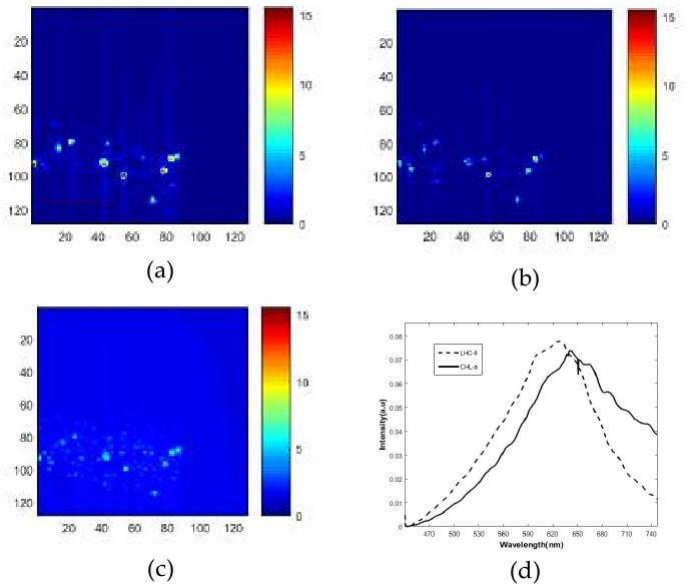

Figure 34 Relative concentration diagram of Chlorella components and their corresponding spectra (a) LHC-II (b) CHl-a (c) Carotenoid (d) Spectral curves corresponding to separated substances.

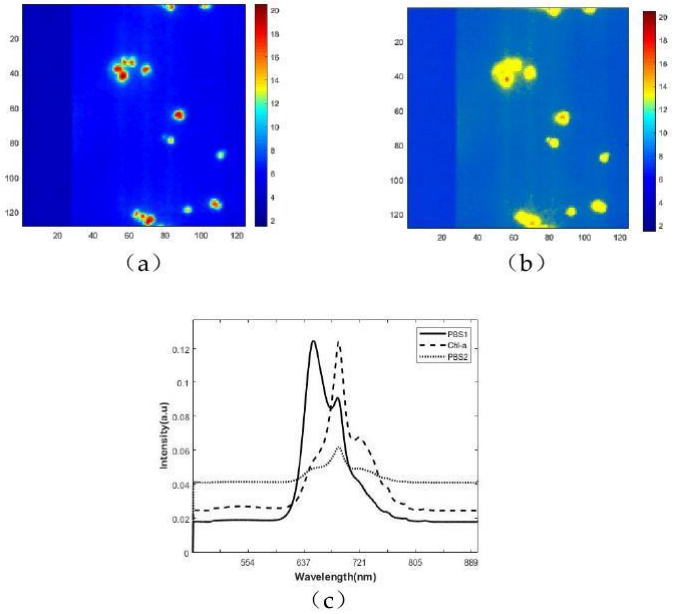

Figure 35 Visual diagram of the main components of Microcystis aeruginosa and its pure spectrum (a) PBS (b) CHl-a (c) Spectral curve.

Compared with Anabaena blooms, the composition characteristics of Microcystis aeruginosa are basically the same, as shown in Figure 34 (a) and (b). The results are consistent with the biological classification of the two algae species - they both belong to cyanobacteria, both contain the same substance phycobilirin and have similar fluorescence characteristics, but from the spectrum, it is found that Anabaena blooms has a single peak while the spectrum of Microcystis aeruginosa has obvious double peaks, as shown in Figure 34(c) the peaks are at 665nm and 654nm, which are basically consistent with the double peaks of the fluorescence spectrum in the previous section, but there is a slight shift. This is due to the system noise in the spectrum measured by hyperspectral and the fluorescence quenching caused by the long excitation time of the microalgae.

Judging from the three sets of data, the spectral analysis results of Anabaena algae and Chlorella are better than those of Microcystis aeruginosa. The reasons may be as follows: The morphology of Microcystis aeruginosa itself is relatively complex. During the growth

1503 Bld. A04, 3rd Software Park, Jimei, Xiamen, 361005, China
Tel: +86-592-6102588

process, the spectral analysis results of It was observed that it was in the shape of a four-leaf clover, and its luminescent substances included phycocyanin, β-carotene and chlorophyll a. The results of this section confirm that hyperspectral imaging technology can not only display the spectral properties of active substances in microalgae cells, but also locate the corresponding luminescent substances. However, if the fluorescent substance is prone to photobleaching under the laser, the fluorescence signal is not strong during the collection process, so the quality of the fluorescence image obtained is not high enough to identify the spectral properties. This shows that this system cannot image cells with strong photobleaching for a long time, and the quality of the fluorescence images collected for some specific algae species is not high, and it cannot be applied to all algae species.

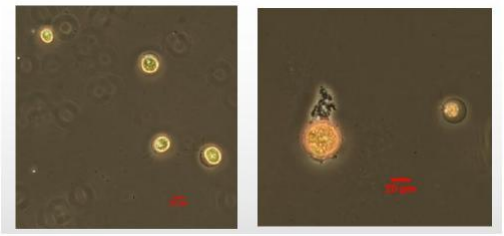

（a） （b）

Figure 36 Haematococcus pluvialis under bright field with 20x objective lens (a) normal condition (b) nitrogen deficiency condition.

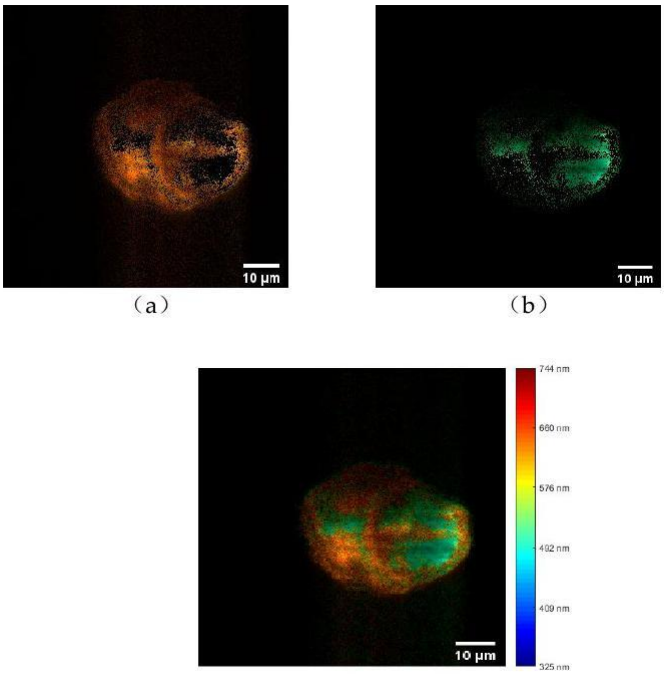

（a） （b）

（c）

Figure 37 Haematococcus pluvialis (a) 576nm-744nm wavelength channel diagram (b) 492nm-576nm wavelength channel diagram (c) Spectral fusion diagram.

Haematococcus pluvialis under extreme conditions, astaxanthin begins to accumulate in the cells due to the lack of nitrogen during cell growth. Channel separation of the hyperspectral fusion image results in Figure 36 (a) and (b), which represent astaxanthin and chlorophyll respectively. The emission spectrum band range of astaxanthin is roughly within 576nm-744nm, based on the basic distribution of astaxanthin in Haematococcus pluvialis cells obtained in (a). At the same time, it was found that during the cell observation process, the chlorophyll content continued to decrease and astaxanthin accumulated, indicating that part of the chlorophyll was converted into astaxanthin under

1503 Bld. A04, 3rd Software Park, Jimei, Xiamen, 361005, China
Tel: +86-592-6102588

nitrogen deficiency conditions.

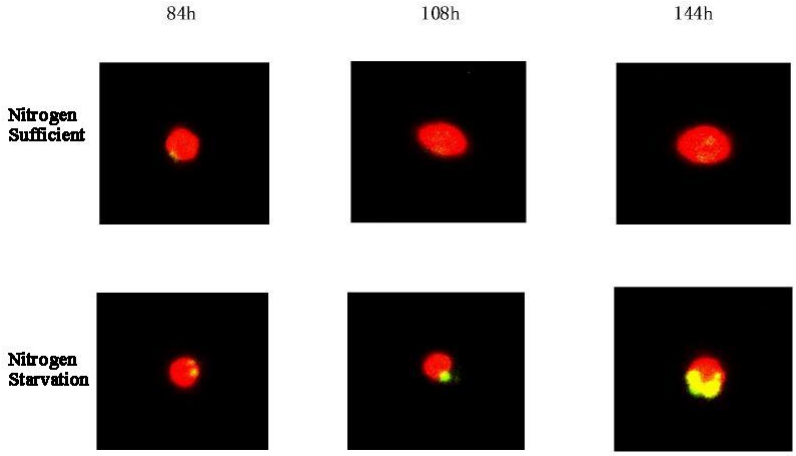

Figure 38 Chlorella lipid growth changes under nitrogen-deficient conditions (a) 84h (b) 108h (c) 144h.

1503 Bld. A04, 3rd Software Park, Jimei, Xiamen, 361005, China
Tel: +86-592-6102588